

# Representing the Dupuit-Boussinesq Aquifer in the National Water Model: Catchment-Scale Application of Hydraulic Groundwater Theory

Minki Hong<sup>1</sup> and Binayak Mohanty<sup>1</sup>

<sup>1</sup>Texas A&M University

November 23, 2022

## Abstract

While hydraulic groundwater theory has been understood as a viable approach for representing the role of the aquifer(s) in the surface-subsurface hydrologic cycle, the integrated modeling community still lacks a proper hydrologic structure to utilize the well-studied theory for large-scale hydrologic predictions. This study aims to present a novel hydrologic modeling framework that enables the Boussinesq equation-based depiction of hillslope-channel connectivity for applying hydraulic groundwater theory to large-scale model configurations. We integrated the BE3S's [Hong et al., 2020] representation scheme of the catchment-scale Boussinesq aquifer into the National Water Model (NWM) and applied the NWM-BE3S model to three major basins in Texas (i.e., the Trinity, Brazos, and Colorado River basins). Since the NWM currently relies on a single reservoir model for baseflow estimation, theory-based evaluation was performed as the efficacies that the Boussinesq aquifer has relative to the single reservoir model should be consistent with hydraulic groundwater theory. We identified that the implemented Boussinesq aquifer(s) showed 'more' pronounced improvements in capturing streamflow dynamics than the original NWM as aquifers exhibited higher nonlinearities in the observed recessions. The varying degree of improvements in streamflow outputs according to the recession nonlinearities demonstrates (1) the applicability of the theory-based depiction of hillslope-channel connectivity and (2) the technical enhancement of model structure. We also examined the river states of all the reaches based on the represented bidirectional lateral hydraulic connections between the stream-aquifer and thus identified the dominant processes between the stream-aquifer (i.e., either river infiltration or baseflow) were spatially variable roughly following climatic gradients.

1     **Representing the Dupuit-Boussinesq Aquifer in the National Water Model:**  
2             **Catchment-Scale Application of Hydraulic Groundwater Theory**

3                             M. Hong<sup>1</sup>, B. P. Mohanty<sup>1</sup>

4     <sup>1</sup>Texas A&M University, Department of Biological and Agricultural Engineering

5     Corresponding author: Binayak P. Mohanty (mailto:bmohanty@tamu.edu)

6  
7  
8     Key Points:

- 9         • Catchment-scale bidirectional lateral hydraulic connections between the stream-aquifer  
10             were newly represented in the National Water Model
- 11         • The Boussinesq aquifer yielded improved streamflow prediction than the single reservoir  
12             model as the nonlinearity of recessions increases
- 13         • The state of river reaches was evaluated based on bidirectional processes by the lateral  
14             hydraulic gradient between the stream-aquifer

24 **Abstract**

25           Although hydraulic groundwater theory has been recognized as a promising tool for  
26 understanding the role of the aquifer(s) in the surface-subsurface hydrologic cycle, the integrated  
27 modeling community still lacks a proper hydrologic structure to apply the well-studied theory to  
28 large-scale hydrologic predictions. This study aims to present a novel hydrologic structure that  
29 enables the Boussinesq equation-based depiction of hillslope-channel connectivity for applying  
30 hydraulic groundwater theory to large-scale model configurations. We integrated the BE3S's  
31 [Hong *et al.*, 2020] representation scheme of the catchment-scale Boussinesq aquifer into the  
32 National Water Model (NWM) and applied the NWM-BE3S model to three major basins in  
33 Texas (i.e., the Trinity, Brazos, and Colorado River basins). Since the NWM currently relies on a  
34 single reservoir model for baseflow simulation, theory-based evaluation was performed as the  
35 efficacies that the Boussinesq aquifer has relative to the single reservoir model should be  
36 consistent/explained with hydraulic groundwater theory. We identified the implemented  
37 Boussinesq aquifer(s) yielded 'more' pronounced improvements in predicting streamflow than  
38 the NWM's bucket model as aquifers exhibited higher nonlinearities in the observed recessions.  
39 The varying degree of improvements in streamflow outputs according to the recession  
40 nonlinearities demonstrates (1) the applicability of the theory-based depiction of hillslope-  
41 channel connectivity as well as (2) the technical enhancement of model structure. We also  
42 diagnosed the river states of all the reaches based on the represented bidirectional lateral  
43 hydraulic connections between the stream-aquifer and identified the dominant processes between  
44 the stream-aquifer (i.e., either river infiltration or baseflow) were spatially heterogenous roughly  
45 following climatic gradients.

46

47

48

49

50

51

## 52 **1 Introduction**

53 Streamflow forecasts have been increasingly gaining attention because of their potential  
54 uses for such as water resources management, reservoir operations, and flood-risk mitigation in  
55 the climate change era [Alfieri *et al.*, 2013; Maurer, 2005; Zhao *et al.*, 2011]. Future water  
56 demand expected to be growing (e.g., crop production) [Rinaudo, 2015] also calls for the  
57 improved streamflow predictability for sustainable use of water resources [Barthel, 2014].  
58 Effective management of water resources should necessitate viable tools, beyond observational  
59 data, to assist decision making, and process-based understanding of dynamic hydrologic systems  
60 has been a fundamental approach for forecasting [Baroni *et al.*, 2019; Jasper *et al.*, 2002;  
61 Maxwell *et al.*, 2015; Viterbo *et al.*, 2020]. Particularly, comprehensive knowledge about large-  
62 scale water cycle/movement can be a basis of holistic communication between different  
63 dimensions (i.e., resources, human, and policy) for socio-economic development [Savenije and  
64 Van der Zaag, 2008].

65 Groundwater and river water are two hydraulically connected reservoirs [Fleckenstein *et al.*  
66 *et al.*, 2010], and thus physically-based simulated streamflow cannot expect significant qualitative  
67 improvements without explicitly accounting for the role of the aquifer in interacting with the  
68 river [Huntington and Niswonger, 2012; Karki *et al.*, 2021; Nijssen *et al.*, 1997]. Over decades, a  
69 variety of efforts has been made to represent the interactive processes between the stream and the  
70 aquifer. The efforts range from building equation-based theoretical method [Boussinesq, 1904;  
71 Hornberger and Remson, 1970; Lockington, 1997; Rorabaugh, 1964; Rupp and Selker, 2005] to  
72 developing integrated hydrologic models with a particular focus on groundwater (GW) - surface  
73 water (SW) interactions [Bisht *et al.*, 2017; Gochis, 2018; Kim *et al.*, 2008; S. J. Kollet and  
74 Maxwell, 2006; C P Shen and Phanikumar, 2010; Tesfa *et al.*, 2014]. Although significant  
75 advances in understanding the effects of GW-SW interactions on streamflow generation have  
76 been achieved by the developed large-scale hydrologic models, particularly, the heterogeneity in  
77 properties and process complexity at different scales still remains as a significant challenge for  
78 an adequate description of exchange processes [Gauthier *et al.*, 2009; Gómez-Hernández and  
79 Gorelick, 1989; Maxwell and Condon, 2016; McDonnell *et al.*, 2007]. Even in (relatively) high-  
80 resolution (e.g., 1-km) integrated models, subsurface heterogeneities ignored below model-

81 specific resolution is one of the primary factors exacerbating the uncertainty in modeled data  
82 [Baroni *et al.*, 2019; S Kollet *et al.*, 2017; Maxwell *et al.*, 2014; Tijerina *et al.*, 2021].

83 To deal with the uncertainty associated with subsurface heterogeneity and dynamics, the  
84 concept of the equivalent parameter (i.e., effective parameter) in reproducing the effects of  
85 subsurface spatial variability has been of critical importance [Berg and Illman, 2011; Binley *et al.*  
86 *et al.*, 1989; Gauthier *et al.*, 2009]. Unlike data-driven parameterization scheme used in several  
87 distributed hydrologic models [Kim *et al.*, 2008; Lautz and Siegel, 2006; Maxwell *et al.*, 2015; C  
88 Shen *et al.*, 2013], no need to characterize (all) relevant small-scale subsurface variations, which  
89 is infeasible due to technological constraints, exists with the working assumption that large-scale  
90 aquifer heterogeneity can be lumped into effective parameter values [Binley *et al.*, 1989;  
91 McDonnell *et al.*, 2007]. However, the scale-dependent nature of aquifer hydraulic properties  
92 (such as saturated hydraulic conductivity  $K_s$  and porosity  $f$ ) requires flux variables observable at  
93 corresponding scale to test if such equivalent properties properly represent natural heterogeneous  
94 system [Dewandel *et al.*, 2017; Fallico *et al.*, 2016; Gómez-Hernández and Gorelick, 1989; Shin  
95 *et al.*, 2013; Zhu and Mohanty, 2003]. Effective parameterization schemes should thus have  
96 limited practical value if flux observations are not readily available at the scale where they  
97 pursue to decide aquifer properties for numerical predictions.

98 The importance of representing catchment-scale hydrologic processes has been studied in  
99 great detail, primarily based on the mathematical relationship between power-law streamflow  
100 recession model and the Boussinesq equation for aquifer outflow [Brutsaert and Nieber, 1977;  
101 Clark *et al.*, 2009; Fan *et al.*, 2019; Troch *et al.*, 2003; Troch *et al.*, 2013; Wagener *et al.*, 2007].  
102 By providing the physically explicit method to explain observed hydrologic responses on  
103 catchment-scale (e.g., groundwater release from hillslope) with catchment (flux) observations  
104 (e.g., streamflow), the theory has enabled not only inferring dominant catchment processes but  
105 also effective parameterization of catchment-scale aquifer [Brutsaert and Lopez, 1998; Vannier  
106 *et al.*, 2014]. While the hillslope-channel exchange representation based on the hydraulic  
107 groundwater theory provides conceptual clarity and parametric efficiency [Fan *et al.*, 2019;  
108 Troch *et al.*, 2013] with (readily available) streamflow observations, integrated modeling  
109 community still lacks an appropriate hydrologic structure (i.e., physics) able to perform theory-  
110 based depiction of hillslope-channel connectivity (e.g., GW-SW interactions). Furthermore, the

111 GW-SW interactions described based on (variably saturated) 2D/3D Richards' equation is  
112 assumed to occur in the vertical direction only [*Bisht et al.*, 2017; *Kim et al.*, 2008; *S. J. Kollet*  
113 *and Maxwell*, 2006; *Seo et al.*, 2007; *Wu et al.*, 2021], which should be considered a structural  
114 limitation that cannot represent the actual GW-SW interactions driven by lateral hydraulic  
115 gradients in real hydrologic systems [*Basha*, 2013; *Boussinesq*, 1904; *Hornberger et al.*, 1970;  
116 *Liang et al.*, 2018; *Paniconi et al.*, 2003; *Rupp and Selker*, 2006].

117 Therefore, this study aims to represent the catchment-scale hillslope-channel connectivity  
118 (i.e., bidirectional interactions) based on the Dupuit-Boussinesq assumption, hereafter referred to  
119 as the Boussienq aquifer, in an integrated framework. As the theoretical basis of hydraulic  
120 groundwater theory, the Boussinesq aquifer can describe the hillslope storage and release  
121 dynamics as the response to streamflow variations (i.e., fluctuations) based on catchment-scale  
122 lateral hydraulic gradients [*Hong et al.*, 2020; *Hornberger et al.*, 1970; *Lockington*, 1997; *Rupp*  
123 *and Selker*, 2006]. To understand the effects of the implemented Boussinesq aquifer with regard  
124 to parametric efficiency and prediction accuracy, we specifically selected the National Water  
125 Model (NWM) (i.e., the WRF-Hydro NWM configuration) and attempted to integrate (i.e., full  
126 coupling) the representation scheme of the catchment-scale Boussinesq aquifer presented in the  
127 recent Bidirectional Exchange Scheme in Surface and Subsurface (BE3S) [*Hong et al.*, 2020]  
128 into the NWM.

129 The National Water Model (NWM), as the Next Generation Water Resources Modeling  
130 Framework (Nextgen), has been operating over the conterminous United States (CONUS) since  
131 2016. Streamflow is one of the primary variables forecasted at various time intervals (i.e., 18 hr  
132 (short), 10 d (medium), and 30 d (long)), and thus the importance of proper representation of  
133 aquifer system is pronounced. Currently, the aquifer-channel connectivity in the NWM relies on  
134 a conceptual (i.e., not physically-explicit) storage ( $S$ ) – discharge ( $Q$ ) reservoir model, which  
135 yields baseflow fluxes ( $Q$ ) as the function of groundwater storage ( $S$ ) [*Gochis*, 2018]. While the  
136 conceptual single reservoir model provides computational efficiency, the (almost) linear  
137 behavior between  $S$  and  $Q$  (of the catchment-scale reservoir(s)) in the NWM [*Karki et al.*, 2021]  
138 hampers the predictive capability of the NWM for streamflow with distinct temporal dynamics  
139 (i.e., high nonlinearity in streamflow recessions). Also, since no hydrologic structure exists to  
140 support physically explicit parameterization of aquifer properties, the fitting parameters (to

141 define the exponential relationship between  $S - Q$ ) have to be empirically derived, and the lateral  
142 hydraulic connections between the stream and the aquifer were inevitably ignored [Gochis,  
143 2018].

144 We presented the coupled NWM-BE3S integrated framework to complement the  
145 addressed structural limitations in the (current) single reservoir baseflow module in the NWM.  
146 To comparatively understand the effects of (different) physics configurations of the aquifer  
147 system in large-scale hydrologic modeling, we applied both the NWM-BE3S and the (original)  
148 NWM to three major basins in Texas (i.e., Trinity River, Brazos River, and Colorado River  
149 basins). Streamflow was used as a primary comparison variable considering the availability of  
150 observations and its implication as the main result of aquifer processes in the (hydraulically-  
151 connected) catchment system. As the working hypothesis ((1), (2), and (3)), the effects of the  
152 Boussinesq equation-based depiction of hillslope-channel connectivity in the NWM-BE3S  
153 coupled model (compared to the original NWM) are evaluated based on the following criteria:

154 (1) The Boussinesq aquifer enables the utilization of effective aquifer parameters (from  
155 streamflow observations) to depict catchment-scale hillslope-channel connectivity.

156 (2) The baseflow fluxes derived from the Boussinesq aquifer should capture a broader  
157 range of streamflow recession characteristics than the single reservoir model.

158 (3) The river states (i.e., gaining/losing) are temporally dynamic and can be diagnosed  
159 based on the lateral hydraulic gradients per the stream-aquifer head difference.

## 160 **2 Methods**

### 161 *2.1 Algorithmic Description of the BE3S*

162 The BE3S couples 1-dimensional governing equations of Richards' equation, Boussinesq  
163 equation, and Saint-Venant equation to represent flow processes in the vadose zone, the phreatic  
164 aquifer, and the open channel (i.e., river reach), respectively. A complete coupled surface-  
165 subsurface flow system should include surface and subsurface hydrologic components,  
166 interfacial/external boundary conditions, and initial conditions in the forward modeling  
167 framework [Furman, 2008]. Time-dependent hydrologic states in each flow domain (e.g.,  
168 groundwater depth and river stage) were explicitly used in establishing interfacial boundary

169 conditions between adjacent domains. The BE3S connects two types of interfaces (i.e., the  
 170 interface between vadose zone-aquifer and aquifer-river) and simulates the potential-driven  
 171 bidirectional exchanges at the interfaces through (hydraulic) head-based boundary conditions  
 172 [Hong *et al.*, 2020]. Since the BE3S handles multiple processes that involve different temporal  
 173 scales ranging from an hour to years, besides, care needs to be taken when defining initial and  
 174 boundary conditions at  $j+1$  th time step as the result of various hydrologic states and fluxes at  $j$   
 175 th time step. Details about the temporal coupling at an hourly time step, the temporal scale in this  
 176 study, are given in Supplemental Information SI1.

### 177 2.1.1 Boussinesq Equation-Based Aquifer System Representation

178 The BE3S solves the non-linear Boussinesq equation, derived from the Dupuit-  
 179 Forcheimer assumption, to represent catchment outflow (i.e., baseflow) as the phreatic aquifer's  
 180 response to a drawdown of river stage [Basha, 2013; Hornberger and Remson, 1970;  
 181 Hornberger *et al.*, 1970; Lockington, 1997]. The non-linear form of the Boussinesq equation was  
 182 applied in a direction perpendicular to the flow direction of the river and incorporates the time-  
 183 dependent river stage as the time-varying boundary condition at the discharge boundary (i.e., the  
 184 interface between the river and the phreatic aquifer) (Figure 1 a). The outflow fluxes from the  
 185 Boussinesq aquifer, therefore, were modeled based on the (time-varying) lateral hydraulic  
 186 gradients between the river stage and adjacent groundwater level (GWL). The hybrid  
 187 discretization scheme (i.e., finite volume and difference) in BE3S also enables an efficient node  
 188 configuration for solving the head-based Boussinesq equation applied with river stage boundary  
 189 conditions (Figure 1 d) (Equation 1, and 2).

$$190 \quad f \times \left[ \frac{h_i^{j+1} - h_i^j}{\Delta t} \right] = \frac{K_s}{\Delta x} \left[ h_i^j \left( \frac{h_{i+1}^j - h_i^j}{\Delta x} \right) - h_{i-1}^j \left( \frac{h_i^j - h_r^j}{\Delta x} \right) \right] \quad (i = 1) \quad (1)$$

$$191 \quad f \times \left[ \frac{h_i^{j+1} - h_i^j}{\Delta t} \right] = \frac{K_s}{\Delta x} \left[ h_i^j \left( \frac{h_{i+1}^j - h_i^j}{\Delta x} \right) - h_{i-1}^j \left( \frac{h_i^j - h_{i-1}^j}{\Delta x} \right) \right] \quad (i = 2, \dots, n_p) \quad (2)$$

192 Where  $h_i^j$  is the hydraulic head of GWL at  $j$  th time step on  $i$  th node (L).  $h_r^j$  is the river  
 193 stage at  $j$  th time step (L).  $f$  is effective porosity (-), and  $K_s$  is horizontal hydraulic conductivity  
 194 ( $\text{LT}^{-1}$ ).  $\Delta x$  is the size of a grid cell in the phreatic aquifer (L).  $n_p$  is the minimum number of

195 aquifer grids from the river reach to the farthest aquifer grid, determined by the corresponding  
 196 catchment's size. The BE3S incorporates the effects of the unsaturated soils on the groundwater  
 197 storage in setting up the initial conditions of Equation 1 and 2 (Figure 1 c), through the  
 198 interfacial boundary equation between the vadose zone and the phreatic aquifer (Equation 3).

$$199 \quad D_i^{j+1} = h_i^j - \left( \frac{f_{vp}^{j+1} \times f}{A_v} \right) \quad (3)$$

200 Where  $D_i^{j+1}$  is the temporary groundwater level hydraulic head used to setup the initial  
 201 condition (i.e., the horizontal profile of saturated aquifer thickness) (L). Again,  $h_i^j$  is the  
 202 hydraulic head of groundwater level at  $j$  th time step on  $i$  th node from the river (L), and  $f$  is the  
 203 effective porosity of the phreatic aquifer.  $A_v$  is the area of an aquifer grid cell ( $L^2$ ).  $f_{vp}^{j+1}$  denotes  
 204 the net exchange fluxes between the unsaturated zone and the phreatic aquifer during  $j+1$  th time  
 205 step. The value distributions of  $D$  were developed based on the distance from the river reach  
 206 (Figure 1 b). For example,  $D_5^j$  is a set of  $D$  values at five grids away from the river at  $j$  th time  
 207 step. Then, the expectation of  $D_i$ , denoted as  $E[D_i]$ , was computed using the probabilistic plot of  
 208 each  $D_i$  ( $i=1,2,\dots,n_p$ ). The estimated  $E[D_i]$  ( $i=1,2,\dots,n_p$ ) was used to set up the initial condition of  
 209 the Boussinesq equation (Figure 1). The boundary forcing at the discharge interface  $h_r^j$  was  
 210 decided by averaging the river stage profile from the most upstream node to the downstream  
 211 node at the corresponding time step. The horizontal profile of groundwater level heads  $h_i^j$

212 ( $i=1,2,\dots,n_p$ ) from the discharge interface to the edge of the catchment on  $j$  th time step was then  
 213 finalized through Equation 1, and 2.

#### 214 2.1.2. Interactions Based on Lateral Hydraulic Connections Between the River and the Aquifer

215 The amount of exchange fluxes between the hillslope and the river channel  $f_{pr}$  were  
 216 computed based on the lateral hydraulic gradients, resulting from the (temporally dynamic) head  
 217 differences between river stage and GWL (Equation 4).

$$218 \quad f_{pr}^j = \begin{cases} K_s \times \left[ (W_p^j) \times \left( \frac{h_r^j - h_{M_r}^j}{M_r} \right) \right] \times n_r \Delta t & (h_{M_r}^j > M_r) \\ K_s \times \left[ (W_p^j) \times \left( \frac{h_r^j - M_r}{M_r} \right) \right] \times n_r \Delta t & (h_{M_r}^j \leq M_r) \end{cases} \quad (4)$$

219 Where  $f_{pr}^j$  is the cumulative exchange fluxes at  $j$  th time step ( $L^3$ ),  $M_r$  is the thickness of  
 220 river bottom sediment (L),  $h_{M_r}^j$  is the hydraulic head of GWL at the distance of  $M_r$  from a river  
 221 channel at  $j$  th time step (L).  $W_p^j$  is the bottom width of the river (L), which varies with the time-  
 222 dependent river stage  $h_r^j$ .  $n_r$  is the number of the river grid cells from the inlet to the outlet of the  
 223 catchment. For simplicity, the thickness of river bottom sediment  $M_r$  was considered equal to the  
 224 size of one grid cell (i.e., 50 m) in the groundwater domain. The mass balance in groundwater  
 225 storage at  $j$  th time step  $S_{gw}^j$  was defined by  $S_{gw}^j = \sum_{i=1}^{n_p} A_p \times h_i^j$ , where  $A_p$  is the area of an  
 226 aquifer grid. The mass balance in the groundwater storage is estimated by Equation 5, and 6.

$$227 \quad \epsilon_{gw}^{j+1} = \left| S_{gw}^{j+1} - \left( S_{gw}^j + \frac{dS_{gw}}{dt} \right) \right| \quad (5)$$

$$228 \quad \frac{dS_{gw}}{dt} \Big|_{t=j} = \sum_{j=1}^{n_p} \nabla f_{vp,j}^j - \nabla f_{pr}^j \quad (6)$$

229 Where  $\epsilon_{gw}^j$  denotes the mass balance in groundwater storage.  $\frac{dS_{gw}}{dt} \Big|_{t=j}$  is considered as  
 230 the result of net exchange fluxes between the vadose zone-the aquifer  $\nabla f_{vp}^j$  and the aquifer-the

231 river  $\nabla f_{pr}^j$ . Errors in aquifer mass balance while simulating  $f_{pr}$  are kept below 0.01 % of the total  
232 volume of groundwater storage.

## 233 2.2 The National Water Model (NWM) Configuration

234 The core of the National Water Model (NWM) system is the National Center for  
235 Atmospheric Research (NCAR)-supported Weather Research and Forecasting Hydrologic  
236 (WRF-Hydro) model [Gochis, 2018]. The WRF-Hydro NWM configuration was developed to  
237 model land surface processes (e.g., water/energy balance) with the Noah-MP (Multi-  
238 Parameterization) model, utilizing NLDAS-2 hourly forcing and 1-km NRCS State Soil  
239 Geographic (STATSGO2) data for soil parameterization [Salas *et al.*, 2018; Schwarz *et al.*,  
240 2018]. The NWM integrates separate routing options for representing subsurface flow for  
241 exfiltration calculation, overland diffusive flow, conceptual bucket baseflow, and open channel  
242 flow (i.e., Muskingum-Cunge routing). The NWM also provides capabilities to simulate  
243 (relatively simple) lake and reservoir surface routing, albeit not activated in this study. Here, we  
244 selectively focus on describing how the connectivity between the open channel and the aquifer is  
245 described using the conceptual storage-discharge bucket model to comparatively understand its  
246 physics differences against the Boussinesq aquifer flow assumption (presented in the BE3S).

### 247 2.2.1 Conceptual Storage-Discharge Bucket Model in the NWM

248 Each river reach has an associated storage-discharge bucket model. The groundwater  
249 discharge (i.e., baseflow), which contributes to the total streamflow, was calculated through the  
250 exponential functionality between the groundwater storage and discharge (Equation 7).  
251 Hereinafter the NWM's bucket model is referred to as Non-linear Single Reservoir, NLSR.

$$252 \quad B_f^j = C \times (e^{\exp \times (\frac{z^j}{z_{max}})} - 1) \quad (7)$$

253 Where  $B_f^j$  is the baseflow fluxes at  $j$  th time step ( $L^3T^{-1}$ ),  $C$  ( $L^3T^{-1}$ ) and  $\exp$   
254 (dimensionless) are calibration 'fitting' parameters.  $z^j/z_{max}$  is the relative groundwater height as  
255  $z^j$  is the groundwater height in the bucket, and  $z_{max}$  is the maximum bucket height, so that each  
256 NLSR has a specified volumetric capacity. The bottom drainage fluxes from the soil columns,

257 included in the corresponding catchment, are aggregated at each time step (hourly) and  
258 accounted for as NLSR inflow (i.e., groundwater recharge) to determine time-dependent  $z^j$  (L).

259 As currently implemented, the NWM does not allow for losses from the channel because  
260 the baseflow is just a function of groundwater storage (i.e., NLSR height,  $z$ ). The river reaches  
261 are thus always considered gaining reaches due to the structure allowing 'only' one-way  
262 exchanges from the NLSR to the river reach. This simplified baseflow estimation is also not a  
263 physically explicit representation of the aquifer system, so the fitting parameters must be  
264 introduced (i.e.,  $C$  and  $exp$  in Equation 7) and empirically derived (for all the catchments). More  
265 importantly, as reported in other studies [Karki *et al.*, 2021], two things should be noted about  
266 the characteristics of the modeled baseflow in the NWM: (a) the lack of groundwater storage is  
267 found in most NLSR(s), meaning the total amount of NLSR inflow (i.e., soil bottom drainage) is  
268 almost identical to that of NLSR outflow (i.e., baseflow), (b) almost no time lag (mostly less  
269 than 1 hours) between the aquifer inflow and outflow is found. The (almost) linear relationship  
270 between the river discharge  $Q$  and groundwater storage  $S$  (i.e.,  $Q \cong S$ ) thus could be concluded  
271 from the current NLSR configuration as the result of the above two factors (a) and (b).

272 However, the baseflow estimation that relies on the relationship  $Q \cong S$  inevitably should  
273 have a structural constraint that cannot depict the streamflow recessions showing high(er)  
274 nonlinearity (e.g., recession slope  $b > 1.0$ ) [Clark *et al.*, 2009; D Dralle *et al.*, 2015; Rupp and  
275 Selker, 2006]. On the other hand, while the most recent NWM version 2.0 has implemented a  
276 river water infiltration scheme [Lahmers *et al.*, 2019], deactivating the channel percolation  
277 process was considered to meet the aim of our study. This is because: (1) only vertical channel  
278 infiltration was accounted for under the assumption that the stream and the aquifer are  
279 disconnected (e.g., semi-arid/arid), (2) lateral hydraulic connections (i.e., GW-SW) were still  
280 ignored so physically-explicit aquifer parameterization is not feasible, and river water infiltration  
281 due to river stage rising (e.g., storm events) cannot be represented [Liang *et al.*, 2018].

### 282 *2.3 Representing the Dupuit-Boussinesq Aquifer System in the NWM Configuration*

283 As an alternative representation of the aquifer system to the NLSR, the Boussinesq  
284 formulation is integrated to the NWM configuration. The coupled NWM-BE3S model was  
285 developed by implementing the parsimonious scheme for the Boussinesq aquifer representation

286 in the BE3S into the framework of the WRF-Hydro configuration for the NWM. The represented  
287 Boussinesq aquifer(s) in the coupled NWM-BE3S model uses the soil bottom drainage modeled  
288 by the Noah-MP LSM and simulates catchment-scale lateral GWL profiles. Unlike the NLSR  
289 baseflow module, the river stage (simulated by the channel routing module) was explicitly  
290 incorporated into the (newly implemented) Boussinesq aquifer module to force the discharge  
291 boundary, and the exchange fluxes (between the stream-aquifer) are calculated bidirectionally  
292 according to lateral hydraulic gradients between the reach and adjacent aquifer (i.e., riparian  
293 zone). Since the framework of the Noah-MP LSM, as coupled with other routing schemes, was  
294 preserved in the NWM-BE3S model, both the NWM and the NWM-BE3S run on the same  
295 meteorological forcing (e.g., NLDAS-2) and soil/terrain routing parameters. The feature of the  
296 NHDPlus WBD that one reach corresponds to one catchment (i.e., connectivity from catchment  
297 to river reach) provided an appropriate structure for setting and solving the distance-based  
298 Boussinesq equation (Equation 1 and 2) in each catchment.

299         The coupled NWM-BE3S generated the bidirectional exchange fluxes (i.e., positive  $f_{pr}$  –  
300 baseflow, negative  $f_{pr}$  – river water infiltration) as the result of lateral hydraulic gradients  
301 (between the river and the riparian zone) on catchment-scale. The  $f_{pr}$ , along with the modeled  
302 overland flow, was ingested in the channel routing module, and the streamflow fluxes were  
303 predicted following the reach-based NHDPlus ver2.0 channel network. By incorporating  
304 physically-based aquifer representation, which stems from the Dupuit-Forcheimer assumption,  
305 importantly, we established the theoretical basis for effective parameterization of the catchment-  
306 scale aquifer (i.e., hydraulic groundwater theory) in the NWM-BE3S model. The effective  
307 aquifer properties  $K_s$  and  $f$ , explicitly used in calculating  $f_{pr}$  (Equation 4), can be inferred from the  
308 analysis of observed streamflow recessions [*Brutsaert and Nieber, 1977; Brutsaert and Lopez,*  
309 *1998; Rupp and Selker, 2006; Troch et al., 1993; Troch et al., 2013*]. Furthermore, since the  
310 framework between the Boussinesq equation and power-law model [*Brutsaert and Nieber, 1977;*  
311 *Szilagyi et al., 1998; Tallaksen, 1995*] provides the theoretical basis of various nonlinearity in the  
312 recessions (compared to the single (non-)linear reservoirs), the NWM-BE3S also provides a  
313 hydrologic structure for depicting streamflow with various recession nonlinearities. The  
314 differences in model physics configuration for the aquifer representation were summed up and  
315 presented in Table 1.

## 316 2.3 Streamflow Recession Analysis for Effective Parameterization of Catchment-Scale Aquifer

317 The mathematical relationship between the Boussinesq aquifer outflow and power-law  
318 model for streamflow recession (i.e., hydraulic groundwater theory) provides a unique physically  
319 explicit method, to date, for inferring catchment-scale effective aquifer properties based on  
320 average baseflow characteristics. In this section, we presented one approach to recession analysis  
321 for effective parameterization using daily streamflow observations, including 1) the recession  
322 extraction, 2) the recession parameter fitting, and 3) selected analytical solutions for each time  
323 domain (i.e., early and late time).

### 324 2.3.1 Recession Extraction Method

325 The criteria for identifying individual recession event (RE) include: 1) the onset of an  
326 individual recession event (RE) was defined as one day (24 hr) after the streamflow peak,  
327 following other studies, to exclude the effects of storm-related flow (e.g., overland flow/quick  
328 subsurface flow) on the streamflow [Biswal and Marani, 2010; Shaw and Riha, 2012], 2) each  
329 RE ends when the daily discharge is at the lowest based on the consecutive decline of discharge  
330 data (i.e.,  $dQ/dt < 0$ ,  $t=1d$ ), and 3) the recession should last more than five days [Biswal and  
331 Marani, 2010; Jachens et al., 2020; Shaw and Riha, 2012].

### 332 2.3.2 Estimation of Recession Parameters

333 Two recession parameters in the power-law model (Equation 8), intercept parameter  $a$   
334 and slope parameter  $b$ , were estimated based on the aggregation of all observed recession data  
335 (i.e., point cloud).

$$336 \quad \frac{dQ}{dt} = -aQ^b \quad (8)$$

337 Where  $Q$  is streamflow ( $L^3T^{-1}$ ), and  $t$  is 1 day. While individual recession analysis could  
338 outperform in analyzing the variability in catchments' response to storm events with different  
339 magnitudes [Jachens et al., 2020; Karlsen et al., 2019; Shaw and Riha, 2012; Szilagyi et al.,  
340 1998; Tashie et al., 2020], we understood the point cloud data is still the only physically-explicit  
341 approach to determine 'average' characteristics of aquifer outflow. As presented by Brutsaert and  
342 Nieber [1977], we considered the lower envelope (LE) of the point cloud recession data under

343 the assumption that small values of  $dQ/dt$  for a given  $Q$  represent the Boussinesq aquifer outflow  
 344 [Brutsaert and Lopez, 1998; Troch et al., 1993; Vannier et al., 2014]. Thus, the recession  
 345 parameter  $b$  was fixed to 3.0 and 1.5 for early time and late time domain, respectively [Brutsaert  
 346 and Nieber, 1977], and  $a$  was determined such that 5 % of points were below the lower envelope  
 347 [Troch et al., 1993; Wang, 2011]. An alternative fitting method, wherein slope parameter  $b$  was  
 348 decided as the best-fitted line to the point cloud, to understand the central tendency (CT) of the  
 349 recession data (while addressing the undue weight of extreme data point) was also utilized  
 350 [Vogel and Kroll, 1992]. The two fitting methods LE and CT were used to determine the  
 351 catchment-scale aquifer properties (e.g.,  $K_s$  and  $f$ ) (LE method), and to represent the average  
 352 catchments' response to storm events during the corresponding period (CT method).

### 353 2.3.3 Catchment-Scale Aquifer Parameterization

354 We selected analytical solutions for the respective early (i.e., high flow) and late time  
 355 domain (i.e., low flow) to determine the catchment-scale aquifer properties under given recession  
 356 parameters  $a$  and  $b$  (estimated through the LE method). The selective use of the recession  
 357 parameters from the LE method reflects our effort to exclusively account for the low-flow  
 358 conditions to infer the aquifer properties. The selected analytical solutions for early time  
 359 [Polubarinova-Koch, 2015] (Equation 9) and late time domain [Boussinesq, 1904] (Equation 10)  
 360 are described below.

$$361 \quad \frac{dQ}{dt} = \frac{1.133}{K_s f D_{ini}^3 L^2} Q^3 \quad (9)$$

$$362 \quad \frac{dQ}{dt} = \frac{4.804 K_s^{1/2} L}{f \alpha^{3/2}} Q^{3/2} \quad (10)$$

363 Where  $K_s$  is the horizontal saturated hydraulic conductivity ( $LT^{-1}$ ),  $f$  is the catchment-  
 364 scale effective porosity (-),  $D_{ini}$  is the initial saturated aquifer thickness (L),  $L$  is the channel  
 365 length (L).  $\alpha$  is the size of (effectively) contributing aquifer during the recessions. Since the size  
 366 of contributing aquifer  $\alpha$  and the initial saturated aquifer thickness  $D_{ini}$  are the two factors that  
 367 affect the diffusivity between the stream and the aquifer, the range of  $\alpha$  and  $D_{ini}$  should be  
 368 adequately determined for realistic estimates of catchment-scale  $K_s$  and  $f$ . Specifically, the  
 369 diffusivity  $K_s/f$  increases (non-linearly) with the increasing size of contributing aquifer and

370 decreases (non-linearly) with increasing  $D_{ini}$  conditions. Thus, the upper and lower bound of  $D_{ini}$   
371 and  $\alpha$  were set up to meet these two criteria: 1) the effective porosity  $f$  should range from 0.1 %  
372 to 20.0 %, 2) the catchment-scale effective horizontal  $K_s$  should be less than  $0.01 \text{ ms}^{-1}$ . Once the  
373 range of  $K_s$  and  $f$  values was determined for each of the 40 catchments, the geometric mean of the  
374 respective range of  $K_s$  and  $f$  was calculated and considered as the representative value of  
375 effective  $K_s$  and  $f$  for the corresponding catchment.

#### 376 *2.4 Comparison Domain*

377 The suitability of the newly represented Boussinesq formulation was evaluated based on  
378 the comparison between the respective streamflow outputs from the retrospective run of the  
379 NWM and the NWM-BE3S model. Both models were run for two years from 1/1/2016 –  
380 12/31/2017, while the first year 2016 (365 d) was considered model spinning, and the modeled  
381 streamflow during the year 2017 (365 d) was used for the evaluation. Both models used the same  
382 hourly NLDAS-2 historic meteorological forcing and produced modeled outputs at hourly  
383 temporal resolution. Two statistical metrics of Pearson's correlation coefficient  $R$  and Root Mean  
384 Square Error ( $RMSE$ ) were used to evaluate the temporal agreement of the respective modeled  
385 streamflow against corresponding observations ( $R$ ) and the amount errors ( $RMSE$ ).

### 386 **3 Study Area and Data Description**

#### 387 *3.1 Study Area*

388 Three major basins in Texas, the Trinity River, the Brazos River, and the Colorado River  
389 basins, are selected as the study areas of this study (Figure 2). The combined area of the three  
390 basins accounts for 37.3 % of the entire Texas area, and the basins are essential sources of water  
391 for most major cities, meandering southeast. The drainage areas are  $40,380 \text{ km}^2$  (1,140 km long),  
392  $116,000 \text{ km}^2$  (1,352 km long), and  $103,000 \text{ km}^2$  (1,378 km long) in the Trinity River, Brazos  
393 River, and Colorado River Basin, respectively. According to the climate classification map, the  
394 northwestern regions of the Colorado River and the Brazos River belong to semi-arid climates.  
395 In contrast, the rest of the two Basins (i.e., southeastern) and the entire Trinity River Basin  
396 belong to the Humid Subtropical climate [Kottek *et al.*, 2006]. Lower annual precipitation is  
397 observed in areas closer to headwater (from the basin outlet). The average annual precipitation  
398 (over the last 30-year) in the Trinity River approximately ranges from 813 mm (i.e., headwater, -

399 98°53'31", 33°37'25") to 1,494 mm (i.e., outlet -98°31'58", 33°21'43"), from 454 mm (i.e.,  
400 headwater, -103°22'40", 34°28'30") to 1,338 (i.e., outlet -95°25'12", 28°59'38") in the Brazos  
401 River, and from 408 mm (i.e., headwater, -103°28'22", 33°17'27") to 1,106 mm (i.e., outlet -  
402 95°59'10", 28°43'05") in the Colorado River basin. Consistent with the precipitation gradient,  
403 which becomes more humid in areas from headwater to the outlet in each basin, the groundwater  
404 depths in the northwestern part of the study areas are deeper than 30 m. In contrast, the relatively  
405 shallower groundwater depths, ranging from 15 m to 3 m, are observed in the southeastern parts  
406 of the study areas.

### 407 *3.1.1 Catchment Delineation*

408 The study area consists of 73,436 catchments, delineated by the NHDPlus (Ver2.0)  
409 Watershed Boundary Dataset (WBD), following the current WRF-Hydro NWM configuration.  
410 As an integrated suite of application-ready geospatial datasets that incorporates many of the  
411 features of the National Hydrography Dataset (NHD) and the National Elevation Dataset (NED),  
412 the NHDPlus WBD includes a stream network based on the medium resolution 1:100,000 scale  
413 and elevation-derived catchments to enforce hydrologic divides (i.e., catchment drainage area).  
414 In this work, the groundwater divides were assumed to follow the boundaries of catchments  
415 since groundwater divides are likely to coincide with regional topographic highs [Anderson *et*  
416 *al.*, 2015]. The catchment boundaries were thus used to delineate the groundwater divides, which  
417 is assumed to be zero-flux BC (i.e., no water crosses a groundwater divide line).

### 418 *3.1.2 Meteorological Forcing*

419 For the two-year 2016 to 2017 retrospective simulation, the North American Land Data  
420 Assimilation System (NLDAS)-2 historical meteorological forcing data were applied to the  
421 original NWM and the coupled NWM-BE3S. As the aim of this study is to selectively evaluate  
422 the improvements in predictive performance by the structural change in the conceptual aquifer  
423 system, we applied the same NWM forcing to both modeling configurations (i.e., the NWM and  
424 the NWM-BE3S models). The NLDAS-2 were in 1/8<sup>th</sup>-degree grid spacing and range from  
425 1/1/1979 to present on an hourly basis. To match the Noah-MP land surface model's spatial  
426 resolution, the NLDAS-2 forcing data were spatially downscaled (re-gridded) at 1-km using  
427 bilinear interpolation for the meteorological variables (e.g., precipitation rate, wind speed,

428 temperature, and long/shortwave radiations) and used to force the upper boundary conditions of  
429 each 1-km land grid.

### 430 *3.1.3 Soil Properties*

431 The United States Geological Survey (USGS) developed the spatial dataset that  
432 represents soil texture attributes, as processed from STATSGO2 database, compiled for the  
433 spatial component of the NHDPlus v2.0 data for the conterminous United States (CONUS)  
434 [Schwarz *et al.*, 2018; Wieczorek and LaMotte, 2010]. Sourcing the STATSGO2 soil data, the  
435 soil properties (e.g., permeability, percent soils, and bulk density) were estimated/provided as the  
436 minimum/maximum/average three values for the individual catchment. We considered that 1) the  
437 catchment-scale effective aquifer properties (e.g., (horizontal) saturated hydraulic conductivity)  
438 could have a significant relationship with catchment-average soil properties (Table 2), and thus  
439 2) the catchment-scale aquifer properties in ungauged catchments could be predicted from the  
440 catchment-average soil attribute data.

### 441 *3.2 Streamflow Observational Data*

442 We used the observed daily averaged streamflow ( $L^3T^{-1}$ ) from 40 USGS gauges, 15  
443 gauges, 14 gauges, and 11 gauges in the Trinity River Basin, the Brazos River Basin, and the  
444 Colorado River Basin (Figure 2), respectively. The daily streamflow observations during the  
445 simulation period were used 1) to understand the seasonal/annual recession characteristics of the  
446 corresponding catchment (i.e., aquifer), especially the nonlinearity of recession curves, in each  
447 catchment, 2) to infer the catchment-scale effective aquifer properties  $K_s$ ,  $f$ ,  $D_{ini}$ , and  $\alpha$ , and 3) to  
448 evaluate the improved predictive performance of the NWM-BE3S coupled model for streamflow  
449 (compared to the original NWM configuration). The major physical characteristics (necessitated  
450 for the recession analysis/effective parameterization) of the selected 40 catchments were listed  
451 up in Table 2.

## 452 **4 Results and Discussion**

### 453 *4.1 Effective Parameterization of Catchment-Scale Aquifers*

#### 454 *4.1.1 Recession Characteristics*

455 As presented in Figure 3, the point cloud recession characteristics were investigated  
456 based on the identified transition of the hydraulic regimes (i.e., early time to late time domain)  
457 for the selected 40 USGS catchments. Parameter  $a$  and  $b$  were estimated to infer the decline rates  
458 (i.e., intercept  $\log(a)$ ) and the nonlinearity (i.e., slope  $b$ ) of the recessions of the catchments. As  
459 addressed in several studies, we found that the different fitting methods resulted in distinct  
460 values of  $\log(a)$  and  $b$  when applied to the daily streamflow observations [D Dralle *et al.*, 2015;  
461 D N Dralle *et al.*, 2017; Jachens *et al.*, 2020; Stoelzle *et al.*, 2013]. While the values of  $\log(a)$   
462 estimated from the CT method (i.e., CT,  $\log(a)$  mean = -1.96) were generally found higher than  
463 those from the LE method (i.e., LE,  $\log(a)$  mean = -2.56), the values of  $\log(a)$  from the  
464 respective CT and LE methods are reasonably consistent with each other (i.e.,  $R = 0.61$ ). Also,  
465 the comparison of the estimated  $\log(a)$  (from the two fitting methods) against the catchment-  
466 average permeability data revealed a significant linear relationship between them (i.e.,  $\log(a)$   
467 from the CT method:  $R = 0.33$ ,  $\log(a)$  from the LE method:  $R = 0.46$ ) as higher decline rates are  
468 expected in the catchments with higher permeability.

#### 469 4.1.2 Effective Aquifer Parameterization for Catchment-Scale Aquifer

470 We determined the effective aquifer properties  $K_s$  and  $f$  for the 40 catchments by  
471 separating the hydraulic regimes from the early time to late time domain. Since the study areas  
472 (i.e., the three major basins) consist of 73,436 catchments (delineated by the NHDPlus v2.0  
473 WBD dataset) and the Boussinesq aquifer flow is implemented for each catchment, the effective  
474 parameters  $K_s$  and  $f$  must be determined to represent distinct diffusivity conditions (between the  
475 stream and the aquifer) in each catchment. We identified a significant linear relationship between  
476 catchment-average permeability ( $LT^{-1}$ ) and catchment-scale effective  $K_s$  (i.e.,  $R = 0.56$ ). Figure 4  
477 a also shows that the catchment-scale effective  $K_s$  are well included in the 95 % band when  
478 predicted with catchment-average permeability ( $LT^{-1}$ ), providing an empirical basis to determine  
479 the effective  $K_s$  in the ungauged catchments (i.e., 73,436 (total) – 40 (gauged) = 73,396 ungauged  
480 catchments). Since no significant ((non)-linear) relationship was found between catchment-  
481 average soil properties and effective  $f$  across the 40 studied catchments, moreover, we tried to to  
482 identify the probability distribution(s) of the diffusivities (i.e.,  $K_s/f$ ) in the 40 catchments to  
483 examine the value distribution pattern. Figure 4 b shows that the value distribution of diffusivity  
484  $K_s/f$  are more properly represented by the log-normal ( $\mu = -2.25$ ,  $\sigma = 1.22$ ) distribution than

485 normal ( $\mu = 0.19$ ,  $\sigma = 0.23$ ), exponential (scale = 0.19), and gamma (shape = 0.92, scale = 0.21)  
486 distributions. The arithmetic mean of the log-normally distributed diffusivity  $K_s/f$  was then  
487 considered as the representative diffusivity condition of the study area, yielding the diffusivity  
488 value of  $0.022 \text{ ms}^{-1}$ . The effective porosity  $f$  of each catchment was then determined according to  
489 the given diffusivity of  $0.022 \text{ ms}^{-1}$  and the effective  $K_s$  of the corresponding catchment. The  
490 catchment-scale effective aquifer properties including  $K_s$ ,  $f$ ,  $D_{ini}$ , and the size of contributing  
491 aquifer (determined following the presented effective parameterization scheme (section 2.3.3)) as  
492 well as the recession parameters  $a$  and  $b$  for each time domain are presented in Table 3.

#### 493 *4.2 Comparative Evaluation of Baseflow Estimates*

##### 494 *4.2.1 Baseflow Module in the Original NWM and Its Structural Limitations*

495 Before elucidating the similarities and differences between the respective baseflow  
496 estimates from the NWM and the coupled NWM-BE3S model, we first examined how the (one-  
497 way) baseflow fluxes were simulated under the original NWM configuration. It turned out that  
498 there was almost no time lag in the water entering (i.e., recharge) and leaving the NLSR, and  
499 almost all the groundwater recharge (into the NLSR) were discharged to the corresponding reach  
500 in the same time step (Figure 5 a, b, and c). The regression between the yearly cumulative NWM  
501 groundwater recharge ( $L^3$ ) and yearly cumulative NWM baseflow ( $L^3$ ) (during the simulation  
502 period) with the best-fit line yielded  $y = 1.02x - 0.11$  ( $R^2 = 0.998$ ). Considering the lack of  
503 groundwater storage ( $S$ ) in the NLSR(s) (indicated by the small depths in the NLSR(s)), we  
504 could conclude that the NLSR simulates the (one-way) baseflow fluxes almost as a single linear  
505 reservoir while yielding the recession slope parameter  $b$  close to 1.0. In other words, the storage-  
506 discharge relationships in the original NWM physics configuration can be described as  $Q$   
507 (discharge)  $\cong S$  (storage) (consistent with previous studies), and thus the linear regression in the  
508  $dQ/dt - Q$  bi-logarithmic space should yield the slope of 1.0. Consequently, the original NWM  
509 might have good predictive performance for recessions exhibiting linearity but also could show  
510 low performance for recessions with high nonlinearity (i.e., steeper/fast streamflow recessions)  
511 due to the structural limitations in its baseflow module.

##### 512 *4.2.2 Comparisons of the Respective Stream-Aquifer Exchange Fluxes According to Recession* 513 *Slope Characteristics*

514 Based on the understood behavioral characteristics of the baseflow outputs from the  
515 NWM, we compared the respective baseflow estimates from the NWM (i.e.,  $B_f$ ) and the NWM-  
516 BE3S model (i.e.,  $f_{pr}$ ) 1-year retrospective run (2017). This comparison was made for the 40  
517 studied catchments that show distinct recession characteristics (i.e., from linear to highly non-  
518 linear) to investigate the similarities and differences between the respective baseflow estimates  
519 according to recession characteristics. The temporal agreements between the respective baseflow  
520 estimates (during the simulation period) were found higher as the recession slope  $b$  of the  
521 corresponding basin is closer to 1.0. That is, the Pearson's  $R$  value distribution (between the  
522 baseflow outputs from the respective NWM and NWM-BE3S) was higher (i.e.,  $R$  average =  
523 0.67) in the Colorado River basin, which showed the lowest  $b$  value distribution with the average  
524  $b$  of 1.17. Likewise, the lowest correspondence of the baseflow estimates (i.e.,  $R$  average = 0.43)  
525 was found in the Trinity River basin, where the recessions were highly non-linear (i.e., slope  $b$  =  
526 1.52). Figure 6 a provides an insight that the outflow from the Boussinesq aquifer can exhibit  
527 similar temporal dynamics with the baseflow fluxes from the NLSR if one basin, as a linked  
528 hydrologic system, shows a linear relationship between groundwater storage  $Q$  and discharge  $S$   
529 (i.e.,  $b = 1.0$ ) [Clark *et al.*, 2009]. The adaptable predictive capabilities of the Boussinesq aquifer  
530 were thus further supported as the linear recession characteristics could also be depicted by the  
531 Boussinesq aquifer. We found that the Pearson's  $R$  between the baseflow estimates ranged from  
532 0.52 – 0.99 among the catchments where the absolute value ( $b - 1$ ) (i.e.,  $|b-1|$ ) is less than 0.42.  
533 The temporal agreement quickly failed when the absolute value of ( $b - 1$ ) is greater than 0.5,  
534 which means increasing nonlinearity of the recessions. Overall, whether the temporal dynamics  
535 of the respective baseflow outputs agree with each other (or not) was well predicted by the slope  
536 parameter  $b$  value with a non-linear fitting (i.e.,  $R^2 = 0.48$ ) (Figure 6 b).

#### 537 *4.2.3 Bidirectional Exchange Fluxes Estimated Based on Lateral Hydraulic Gradients in the* 538 *NWM-BE3S model*

539 Closer inspection revealed that, furthermore, the sign of the modeled  $f_{pr}$  fluxes, unlike the  
540 (one-way) baseflow fluxes in the NWM, could be either positive (i.e., groundwater discharge to  
541 the river) or negative (i.e., river infiltration to the aquifer) (Figure 7). The negative  $f_{pr}$  physically  
542 means that the rapid rises in the river stage (mostly) by storm events might lead to river water  
543 discharge into the phreatic aquifer [Liang *et al.*, 2018]. These temporary changes in the river

544 states illustrate that the river states need to be understood as temporally dynamic following the  
545 lateral head differences between the river stage and adjacent groundwater level. As we consider  
546 that the groundwater storage is the combinative effects from the vadose zone and the river  
547 channel [Hong *et al.*, 2020], the structural enhancement in the NWM-BE3S to predict the  
548 bidirectional stream-aquifer exchange fluxes is not only capable of allowing channel losses but  
549 also improving the feasibility of the catchment-scale water budget closure.

#### 550 *4.3 Improved Streamflow Predictions*

551 From the understood differences between the modeled outputs  $B_f$  and  $f_{pr}$ , we considered  
552 that the outflow from the implemented Boussinesq aquifer could yield 'more' pronounced  
553 improvements in streamflow predictions as the catchments function as a non-linear reservoir(s)  
554 between  $Q$  and  $S$ . To better evaluate the improvements in the streamflow predictions generated  
555 by the NWM-BE3S (compared to the original NWM), the evaluation of the streamflow outputs  
556 from the respective models against streamflow observations was carried out in consideration of  
557 the variability in the recession nonlinearity, which varies by region and time period.

- 558 1) Since the aquifers in each basin function differently in generating baseflow (i.e., high  
559 nonlinearity – Trinity River basin, low nonlinearity – Colorado River basin), the  
560 improvements in the streamflow predictions should be evaluated by the basin.
- 561 2) Even if it is the same basin, the recession nonlinearity appeared distinctly across time.  
562 We thus divided one year (2017) into four-month periods (i.e., JFMA (1-4), MJJA (5-8),  
563 SOND (9-12)), at which apparent differences in recession slope characteristics were  
564 identified.

565 **Trinity River basin** - The Trinity River basin exhibited the highest nonlinearity in the  
566 recession data among the three study basins (as addressed in section 4.2.2). For the selected 15  
567 catchments in the Trinity River basin, the average  $b$  in each period gradually increased as 1.78 in  
568 JFMA, 2.19 in MJJA, and 2.48 in SOND. When it comes to temporal agreements of the  
569 respective streamflow predictions against the corresponding observations, we found significant  
570 improvements in  $R$  values from all three periods. The average  $R$ -value improves from 0.18  
571 (NWM) to 0.39 (NWM-BE3S) in JFMA period, from 0.23 (NWM) to 0.42 (NWM-BE3S) in  
572 MJJA period, and from -0.02 (NWM) to 0.31 (NWM-BE3S) in SOND period. This is mainly

573 because the recession nonlinearities (of the streamflow observations) from the Trinity River  
574 basin were maintained high throughout the year. We also found significant reductions in the  
575 *RMSE* values across the 15 catchments. The average *RMSE* reduced from 29.1 m<sup>3</sup>hr<sup>-1</sup> (NWM) to  
576 19.8 m<sup>3</sup>hr<sup>-1</sup> (NWM-BE3S) in JFMA period, from 64.0 m<sup>3</sup>hr<sup>-1</sup> (NWM) to 46.7 m<sup>3</sup>hr<sup>-1</sup> (NWM-  
577 BE3S) in MJJA period, and from 32.5 m<sup>3</sup>hr<sup>-1</sup> (NWM) to 21.8 m<sup>3</sup>hr<sup>-1</sup> (NWM-BE3S) in SOND  
578 period.

579 **Brazos River basin** - The average *b* in each period was found lower than those in the Trinity  
580 River, yielding the average *b* of 1.43 in JFMA, 1.19 in MJJA, and 1.66 in SOND. The Brazos  
581 River basin was found to function closest to the linear reservoir during the MJJA (2017) period  
582 (i.e., average *b* of 1.19). The average *R* (for the selected 14 catchments) improved from 0.28  
583 (NWM) to 0.43 (NWM-BE3S) in JFMA period, from 0.35 (NWM) to 0.45 (NWM-BE3S) in  
584 MJJA period, and from 0.02 (NWM) to 0.11 (NWM-BE3S) in SOND period. Consistent with the  
585 trend found in the *b* value distributions, we found minimal improvement in *R* during the MJJA  
586 period compared to other JFMA and SOND periods. We also identified pronounced reductions in  
587 *RMSE* values as the average *RMSE* reduced from 63.8 m<sup>3</sup>hr<sup>-1</sup> (NWM) to 45.9 m<sup>3</sup>hr<sup>-1</sup> (NWM-  
588 BE3S) in JFMA period, from 183.1 m<sup>3</sup>hr<sup>-1</sup> (NWM) to 75.7 m<sup>3</sup>hr<sup>-1</sup> (NWM-BE3S) in MJJA  
589 period, and from 129.9 m<sup>3</sup>hr<sup>-1</sup> (NWM) to 44.6 m<sup>3</sup>hr<sup>-1</sup> (NWM-BE3S) in SOND period.

590 **Colorado River basin** - The trends and value distributions of *b* (for the three periods) in the  
591 Colorado River basin were found similar to those of the Brazos River basin. In the Colorado  
592 River basin, the value distribution of *b* and its average were closest to 1.0 in MJJA period while  
593 the average *b* values during JFMA, and SOND were relatively high (i.e., the average *b* of 1.82 in  
594 JFMA, 1.03 in MJJA, and 1.69 in SOND period). Notably, the average *b* during MJJA in the  
595 Colorado River was 1.03, implying that the corresponding basin functioned almost as a linear  
596 reservoir during that time. The average *R* improved from -0.06 (NWM) to 0.31 (NWM-BE3S) in  
597 JFMA period, from 0.49 (NWM) to 0.50 (NWM-BE3S) in MJJA period, and -0.03 (NWM) to  
598 0.11 (NWM-BE3S) in SOND period. As expected, the average and value distribution of *R*  
599 showed little improvement during the MJJA period, while significantly improved *R* (i.e., average  
600 and value distribution) was found in both JFMA and SOND periods. Like the other two basins,  
601 pronounced reductions in *RMSE* were identified as reducing from 31.5 m<sup>3</sup>hr<sup>-1</sup> (NWM) to 20.8

602  $\text{m}^3\text{hr}^{-1}$  (NWM-BE3S) in JFMA period, from  $74.5 \text{ m}^3\text{hr}^{-1}$  (NWM) to  $49.7 \text{ m}^3\text{hr}^{-1}$  (NWM-BE3S) in  
603 MJJA period, and from  $32.2 \text{ m}^3\text{hr}^{-1}$  (NWM) to  $9.97 \text{ m}^3\text{hr}^{-1}$  (NWM-BE3S) in SOND period.

604 We overall identified that the degree of temporal agreement between the NWM-BE3S-  
605 derived streamflow outputs and corresponding observations was consistent with the trends in the  
606  $b$  value distributions. For both Brazos and Colorado basins, the  $R$  improvements were  
607 little/minimal during MJJA when the basins behaved more like a linear reservoir (i.e.,  $b$  close to  
608 1.0) while significantly improved  $R$  was found in the periods JFMA and SOND. We note that the  
609 improved streamflow predictive skill in the NWM-BE3S (compared to the original NWM) was  
610 also ensured by the value distributions of  $R$  and  $RMSE$  (Figure 8). The improvements (i.e.,  
611 reductions) in  $RMSE$  were found more pronounced during the low-flow conditions (periods) than  
612 high-flow conditions. Since river waters are considered sustained mainly by groundwater  
613 discharge during the low-flow conditions (e.g., low precipitation, extended dry period), the lower  
614  $RMSE$  values during the low-flow conditions showed the suitability of the Boussinesq aquifer  
615 formulation for baseflow estimation (Figure 8). Figure 9 shows comparatively how the dynamics  
616 of the observed streamflow were simulated by the two model NWM and NWM-BE3S,  
617 respectively. Consequently, we identified significant improvements in the streamflow predictions  
618 from the NWM-BE3S in terms of both representing temporal dynamics as well as reducing  
619 amount errors.

620 To clarify the reasons of the improved model performance, we further estimated the  
621 errors in the modeled recession durations derived from both models by comparing them with the  
622 corresponding observed recession durations. Figure 10 showed that the duration of individual  
623 recession events was significantly better represented under the implemented Boussinesq aquifer  
624 in the NWM-BE3S. The recession events were generally predicted longer than the observed  
625 periods in the original NWM, as shown by that the most errors were biased negative. We  
626 understood that the reductions in the duration errors are the results of the adaptable predictive  
627 capabilities of the Boussinesq aquifer formulation (for the recession events with distinct  
628 recession characteristics). This is because the new Boussinesq aquifer module could account for  
629 (rapidly) decreasing baseflow fluxes due to the rapid reductions in the lateral head differences  
630 (between the stream-aquifer) as the recession progresses, which yields higher nonlinearity in the  
631 recessions. Unlike the NLSR model, to sum, the streamflow predictions by the Boussinesq

632 aquifer were found able to represent the distinct recession characteristics observed in the  
633 corresponding (actual) catchment. Consequently, we argue that the newly represented lateral  
634 hydraulic connections (based on the Boussinesq equation) enabled the more accurate  
635 representation of the recessions which start/end based on the lateral hydraulic gradients between  
636 the river stage and water table in the actual catchment system, and thus the applicability of the  
637 Boussinesq aquifer, as an alternative to the current NLSR model, to represent hillslope-channel  
638 interactions is demonstrated.

#### 639 *4.4 Mapping the Examined River States*

640 The NWM-BE3S model can explicitly simulate the bidirectional exchange fluxes  $f_{pr}$   
641 while accounting for the temporal dynamics of the catchment-scale lateral hydraulic gradients.  
642 Here we examined the state of each of the 73,436 river reaches (distributed across the study  
643 basins) based on the yearly cumulative  $f_{pr}$  fluxes over the one-year evaluation period. The  
644 cumulative  $f_{pr}$  provided insight into whether the dominant process (between the stream and the  
645 aquifer) was river water infiltration (i.e., losing reach) or groundwater discharge to the river (i.e.,  
646 gaining stream). Although the states of the channel reaches were always recognized as gaining  
647 reach due to one-way representation of GW-SW exchanges (i.e.,  $B_f$ ) in the (original) NWM,  
648 significant spatial variability/patterns were exhibited by the NWM-BE3S-derived  $f_{pr}$  outputs. The  
649 comparison between the spatial distributions from the cumulative  $B_f$  and  $f_{pr}$  clarified that the  
650 dominant processes between the stream and the aquifer in the 73,436 catchments were spatially  
651 heterogeneous (Figure 11 a, b). The yearly cumulative  $f_{pr}$  values were estimated to be ranging  
652 from  $-1,750 \text{ m}^3$  (negative) –  $1,740 \text{ m}^3$  (positive), while most negative  $f_{pr}$  values (i.e., about 98.8  
653 %) were simulated in the northwestern regions, where the average annual precipitation was only  
654 one-third compared to the southeastern parts. However, Figure 11 b showed that the cumulative  
655  $B_f$  values modeled in the catchments belonging to semi-arid hydroclimate [Kottek *et al.*, 2006]  
656 were found (instead) positively more enormous, which is counter-intuitive, than other parts of  
657 the study area.

658 On the other hand, we also found some similarities between the respective value  
659 distributions of  $f_{pr}$  and  $B_f$ . The yearly cumulative exchange fluxes (i.e., net exchange fluxes)  
660 ranging from  $0.0 \text{ m}^3$  –  $1.0 \text{ m}^3$  were simulated by about half of the catchments from both the  
661 NWM and the NWM-BE3S (i.e., 52.1% in the NWM, and 47.5 % in the NWM-BE3S), and the

662 number of the river reaches was found to decrease exponentially with increasing the (positive)  
663 value of both  $f_{pr}$  and  $B_f$  (Figure 11 c). These similar value distributions, albeit limited for positive  
664 values, were attributed to that the estimation of the exchange fluxes  $f_{pr}$  and  $B_f$  was dependent  
665 upon the size of corresponding catchment/reach (Equation 4) in both configurations of the NWM  
666 and the NWM-BE3S. According to the NWM-BE3S  $f_{pr}$  outputs, we found that river water  
667 infiltration was the dominant process among 10.1 % of the river reaches (i.e., 7,417 reaches)  
668 during the evaluation period 2017.

## 669 **5 Conclusions and Future Work**

670 Although the relevance of hydraulic groundwater theory in understanding the role of the  
671 aquifer(s) in the development of surface-subsurface hydrologic cycle has been addressed over the  
672 past few decades, the lack of an appropriate modeling structure was the primary constraint to  
673 applying the well-studied theory to large-scale hydrologic predictions [*Clark et al.*, 2015; *Fan et*  
674 *al.*, 2019; *Rupp and Selker*, 2006; *Troch et al.*, 2013]. With the aim of representing the theory-  
675 based depiction of GW-SW interactions (i.e., hillslope-stream connectivity) in an integrated  
676 hydrologic model, we established a novel hydrologic framework NWM-BE3S by integrating the  
677 BE3S's Boussinesq equation-based representation of (catchment-scale) aquifer into the NWM.  
678 The applicability of the Boussinesq formulation to large-scale hydrologic predictions was  
679 successfully demonstrated based on the improved predictive performance for streamflow  
680 identified in the NWM-BE3S model. To ensure the validity of groundwater flow based on the  
681 Dupuit-Forcheimer assumption in the large-scale integrated modeling, the primary premise of  
682 our comparative evaluation (between the Boussinesq aquifer and the NLSR) has been that the  
683 effects made by the newly implemented Boussinesq aquifer should be consistent with the theory  
684 (i.e., theory-based evaluation). In this context, the varying degree of improvement in streamflow  
685 predictions (by the NWM-BE3S) according to the recession nonlinearities (i.e., recession slope  
686  $b$ ) manifests (1) the applicability of the theory-based depiction of hillslope-channel interactions  
687 as well as (2) the technical enhancement of model structure.

688 For future work, we will mainly focus on the effects of fluvial system dynamics on  
689 horizontal groundwater redistribution and resultant impacts on land surface water/energy  
690 processes (e.g., atmospheric boundary layers (ABL) processes). While some studies attempted to  
691 understand the interactive relationship between (horizontal) subsurface flow and land surface

692 processes, however, the groundwater flows as the response of fluvial system dynamics has not  
693 been adequately represented in most hydrologic models as well as land surface models (LSMs) /  
694 earth system models (ESMs) [Bisht *et al.*, 2017; Fan *et al.*, 2007; Fan *et al.*, 2019; Gochis, 2018;  
695 Stefan J. Kollet and Maxwell, 2008; Lawrence *et al.*, 2019; Maxwell and Kollet, 2008; Wu *et al.*,  
696 2021]. By representing the bidirectional lateral hydraulic connections between the hillslopes and  
697 the open channel reaches (GW-SW interactions), the presented NWM-BE3S also provides one  
698 unique forward modeling capability to explicitly incorporate the spatiotemporally dynamic  
699 groundwater flow *as the results of bidirectional lateral hillslope-channel connectivity* into land  
700 surface schemes. Relying on understood effects of groundwater dynamics on vadose zone  
701 processes [Hong *et al.*, 2020], we thus aim to comprehensively understand the interaction  
702 patterns (over large areas) between the vadose zone-groundwater-channel that vary according to  
703 climatic/hydro(geo)logic conditions and its resulting impacts on the land surface water/energy  
704 budget (e.g., near-surface soil moisture, and ET) and thus ABL processes.

## 705 **Acknowledgments, Samples, and Data**

706 We acknowledge the funding support from the USDA grant (Project No. 2017-68007-  
707 26318) through the National Institute for Food and Agriculture's Agriculture and Food Research  
708 Initiative, Water for Agricultural Challenge Area, W-4188 multi-state HATCH project, and  
709 USGS TWRI Graduate Research Program. The dataset used in this study are available from the  
710 USGS website for the watersheds in the United States at  
711 <https://maps.waterdata.usgs.gov/mapper/index.html>

## 712 **References**

- 713 Alfieri, L., P. Burek, E. Dutra, B. Krzeminski, D. Muraro, J. Thielen, and F. Pappenberger  
714 (2013), Glofas – Global Ensemble Streamflow Forecasting and Flood Early Warning,  
715 *Hydrology and Earth System Sciences*, 17(3), 1161-1175.
- 716 Anderson, M. P., W. W. Woessner, and R. J. Hunt (2015), *Applied Groundwater Modeling:  
717 Simulation of Flow and Advective Transport*, Academic press.
- 718 Baroni, G., B. Schalge, O. Rakovec, R. Kumar, L. Schüller, L. Samaniego, C. Simmer, and S.  
719 Attinger (2019), A Comprehensive Distributed Hydrological Modeling  
720 Intercomparison to Support Process Representation and Data Collection Strategies,  
721 *Water Resources Research*, 55(2), 990-1010.
- 722 Barthel, R. (2014), Hess Opinions &quot;Integration of Groundwater and Surface Water  
723 Research: An Interdisciplinary Problem?&quot;, *Hydrology and Earth System  
724 Sciences*, 18(7), 2615-2628.

725 Basha, H. A. (2013), Traveling Wave Solution of the Boussinesq Equation for Groundwater  
726 Flow in Horizontal Aquifers, *Water Resources Research*, 49(3), 1668-1679.

727 Berg, S. J., and W. A. Illman (2011), Capturing Aquifer Heterogeneity: Comparison of  
728 Approaches through Controlled Sandbox Experiments, *Water Resources Research*,  
729 47(9), n/a-n/a.

730 Binley, A., K. Beven, and J. Elgy (1989), A Physically Based Model of Heterogeneous  
731 Hillslopes: 2. Effective Hydraulic Conductivities, *Water Resources Research*, 25(6),  
732 1227-1233.

733 Bisht, G., M. Y. Huang, T. Zhou, X. Y. Chen, H. Dai, G. E. Hammond, W. J. Riley, J. L. Downs, Y.  
734 Liu, and J. M. Zachara (2017), Coupling a Three-Dimensional Subsurface Flow and  
735 Transport Model with a Land Surface Model to Simulate Stream-Aquifer-Land  
736 Interactions (Cp V1.0), *Geoscientific Model Development*, 10(12), 4539-4562.

737 Biswal, B., and M. Marani (2010), Geomorphological Origin of Recession Curves,  
738 *Geophysical Research Letters*, 37(24), n/a-n/a.

739 Boussinesq, J. (1904), Recherches the´Oriques Sur L'e´Coulement Des Nappes D'eau  
740 Infiltr'e´es Dans Le Sol Et Sur De´Bit De Sources, *Journal de Mathématiques Pures et*  
741 *Appliquées*, 10, 5-78.

742 Brutsaert, W., and J. L. Nieber (1977), Regionalized Drought Flow Hydrographs from a  
743 Mature Glaciated Plateau, *Water Resources Research*, 13(3), 637-643.

744 Brutsaert, W., and J. P. Lopez (1998), Basin-Scale Geohydrologic Drought Flow Features of  
745 Riparian Aquifers in the Southern Great Plains, *Water Resources Research*, 34(2),  
746 233-240.

747 Clark, M. P., D. E. Rupp, R. A. Woods, H. J. Tromp-Van Meerveld, N. E. Peters, and J. E. Freer  
748 (2009), Consistency between Hydrological Models and Field Observations: Linking  
749 Processes at the Hillslope Scale to Hydrological Responses at the Watershed Scale,  
750 *Hydrological Processes*, 23(2), 311-319.

751 Clark, M. P., et al. (2015), Improving the Representation of Hydrologic Processes in Earth  
752 System Models, *Water Resources Research*, 51(8), 5929-5956.

753 Dewandel, B., Y. Caballero, J. Perrin, A. Boisson, F. Dazin, S. Ferrant, S. Chandra, and J.-C.  
754 Maréchal (2017), A Methodology for Regionalizing 3-D Effective Porosity at  
755 Watershed Scale in Crystalline Aquifers, *Hydrological Processes*, 31(12), 2277-  
756 2295.

757 Dralle, D., N. Karst, and S. E. Thompson (2015), A, B Careful: The Challenge of Scale  
758 Invariance for Comparative Analyses in Power Law Models of the Streamflow  
759 Recession, *Geophysical Research Letters*, 42(21), 9285-9293.

760 Dralle, D. N., N. J. Karst, K. Charalampous, A. Veenstra, and S. E. Thompson (2017), Event-  
761 Scale Power Law Recession Analysis: Quantifying Methodological Uncertainty,  
762 *Hydrology and Earth System Sciences*, 21(1), 65-81.

763 Fallico, C., S. De Bartolo, M. Veltri, and G. Severino (2016), On the Dependence of the  
764 Saturated Hydraulic Conductivity Upon the Effective Porosity through a Power Law  
765 Model at Different Scales, *Hydrological Processes*, 30(13), 2366-2372.

766 Fan, Y., G. Miguez-Macho, C. P. Weaver, R. Walko, and A. Robock (2007), Incorporating  
767 Water Table Dynamics in Climate Modeling: 1. Water Table Observations and  
768 Equilibrium Water Table Simulations, *Journal of Geophysical Research-*  
769 *Atmospheres*, 112(D10).

770 Fan, Y., et al. (2019), Hillslope Hydrology in Global Change Research and Earth System  
771 Modeling, *Water Resources Research*, 55(2), 1737-1772.

772 Fleckenstein, J. H., S. Krause, D. M. Hannah, and F. Boano (2010), Groundwater-Surface  
773 Water Interactions: New Methods and Models to Improve Understanding of  
774 Processes and Dynamics, *Advances in Water Resources*, 33(11), 1291-1295.

775 Furman, A. (2008), Modeling Coupled Surface-Subsurface Flow Processes: A Review,  
776 *Vadose Zone Journal*, 7(2), 741-756.

777 Gauthier, M. J., M. Camporese, C. Rivard, C. Paniconi, and M. Larocque (2009), A Modeling  
778 Study of Heterogeneity and Surface Water-Groundwater Interactions in the Thomas  
779 Brook Catchment, Annapolis Valley (Nova Scotia, Canada), *Hydrology and Earth  
780 System Sciences*, 13(9), 1583-1596.

781 Gochis, D. J., M. Barlage, A. Dugger, K. FitzGerald, L. Karsten, M. McAllister, J. McCreight, J.  
782 Mills, A. RafieeiNasab, L. Read, K. Sampson, D. Yates, W. Yu, (2018), The Ncar Wrf-  
783 Hydro Modeling System Technical Description (Version 5.0), National Center for  
784 Atmospheric Research.

785 Gómez-Hernández, J. J., and S. M. Gorelick (1989), Effective Groundwater Model Parameter  
786 Values: Influence of Spatial Variability of Hydraulic Conductivity, Leakance, and  
787 Recharge, *Water Resources Research*, 25(3), 405-419.

788 Hong, M., B. P. Mohanty, and Z. Sheng (2020), An Explicit Scheme to Represent the  
789 Bidirectional Hydrologic Exchanges between the Vadose Zone, Phreatic Aquifer, and  
790 River, *Water Resources Research*, 56(9).

791 Hornberger, G. M., and I. Remson (1970), A Moving Boundary Model of a One-Dimensional  
792 Saturated-Unsaturated, Transient Porous Flow System, *Water Resources Research*,  
793 6(3), 898-+.

794 Hornberger, G. M., J. Ebert, and I. Remson (1970), Numerical Solution of Boussinesq  
795 Equation for Aquifer-Stream Interaction, *Water Resources Research*, 6(2), 601-+.

796 Huntington, J. L., and R. G. Niswonger (2012), Role of Surface-Water and Groundwater  
797 Interactions on Projected Summertime Streamflow in Snow Dominated Regions: An  
798 Integrated Modeling Approach, *Water Resources Research*, 48(11), n/a-n/a.

799 Jachens, E. R., D. E. Rupp, C. Roques, and J. S. Selker (2020), Recession Analysis Revisited:  
800 Impacts of Climate on Parameter Estimation, *Hydrology and Earth System Sciences*,  
801 24(3), 1159-1170.

802 Jasper, K., J. Gurtz, and H. Lang (2002), Advanced Flood Forecasting in Alpine Watersheds  
803 by Coupling Meteorological Observations and Forecasts with a Distributed  
804 Hydrological Model, *Journal of Hydrology*, 267(1-2), 40-52.

805 Karki, R., J. M. Krienert, M. Hong, and D. R. Steward (2021), Evaluating Baseflow Simulation  
806 in the National Water Model: A Case Study in the Northern High Plains Region, USA,  
807 *JAWRA Journal of the American Water Resources Association*, 57(2), 267-280.

808 Karlsen, R. H., K. Bishop, T. Grabs, M. Ottosson-Löfvenius, H. Laudon, and J. Seibert (2019),  
809 The Role of Landscape Properties, Storage and Evapotranspiration on Variability in  
810 Streamflow Recessions in a Boreal Catchment, *Journal of Hydrology*, 570, 315-328.

811 Kim, N. W., I. M. Chung, Y. S. Won, and J. G. Arnold (2008), Development and Application of  
812 the Integrated Swat-Modflow Model, *Journal of Hydrology*, 356(1-2), 1-16.

813 Kollet, S., et al. (2017), The Integrated Hydrologic Model Intercomparison Project, Ih-Mip2:  
814 A Second Set of Benchmark Results to Diagnose Integrated Hydrology and  
815 Feedbacks, *Water Resources Research*, 53(1), 867-890.

816 Kollet, S. J., and R. M. Maxwell (2006), Integrated Surface-Groundwater Flow Modeling: A  
817 Free-Surface Overland Flow Boundary Condition in a Parallel Groundwater Flow  
818 Model, *Advances in Water Resources*, 29(7), 945-958.

819 Kollet, S. J., and R. M. Maxwell (2008), Capturing the Influence of Groundwater Dynamics on  
820 Land Surface Processes Using an Integrated, Distributed Watershed Model, *Water*  
821 *Resources Research*, 44(2), n/a-n/a.

822 Kottek, M., J. Grieser, C. Beck, B. Rudolf, and F. Rubel (2006), World Map of the Köppen-  
823 Geiger Climate Classification Updated, *Meteorologische Zeitschrift*, 15(3), 259-263.

824 Lahmers, T. M., H. Gupta, C. L. Castro, D. J. Gochis, D. Yates, A. Dugger, D. Goodrich, and P.  
825 Hazenberg (2019), Enhancing the Structure of the Wrf-Hydro Hydrologic Model for  
826 Semiarid Environments, *J. Hydrometeorol.*, 20(4), 691-714.

827 Lautz, L. K., and D. I. Siegel (2006), Modeling Surface and Ground Water Mixing in the  
828 Hyporheic Zone Using Modflow and Mt3d, *Advances in Water Resources*, 29(11),  
829 1618-1633.

830 Lawrence, D. M., et al. (2019), The Community Land Model Version 5: Description of New  
831 Features, Benchmarking, and Impact of Forcing Uncertainty, *Journal of Advances in*  
832 *Modeling Earth Systems*, 11(12), 4245-4287.

833 Liang, X., H. Zhan, and K. Schilling (2018), Spatiotemporal Responses of Groundwater Flow  
834 and Aquifer-River Exchanges to Flood Events, *Water Resources Research*, 54(3),  
835 1513-1532.

836 Lockington, D. A. (1997), Response of Unconfined Aquifer to Sudden Change in Boundary  
837 Head, *Journal of Irrigation and Drainage Engineering*, 123(1), 24-27.

838 Maurer, E. P. (2005), Uncertainty in Projections of Streamflow Changes Due to Climate  
839 Change in California, *Geophysical Research Letters*, 32(3).

840 Maxwell, R. M., and S. J. Kollet (2008), Interdependence of Groundwater Dynamics and  
841 Land-Energy Feedbacks under Climate Change, *Nature Geoscience*, 1(10), 665-669.

842 Maxwell, R. M., and L. E. Condon (2016), Connections between Groundwater Flow and  
843 Transpiration Partitioning, *353(6297)*, 377-380.

844 Maxwell, R. M., L. E. Condon, and S. J. Kollet (2015), A High-Resolution Simulation of  
845 Groundwater and Surface Water over Most of the Continental Us with the Integrated  
846 Hydrologic Model Parflow V3, *Geoscientific Model Development*, 8(3), 923-937.

847 Maxwell, R. M., et al. (2014), Surface-Subsurface Model Intercomparison: A First Set of  
848 Benchmark Results to Diagnose Integrated Hydrology and Feedbacks, *Water*  
849 *Resources Research*, 50(2), 1531-1549.

850 McDonnell, J. J., et al. (2007), Moving Beyond Heterogeneity and Process Complexity: A  
851 New Vision for Watershed Hydrology, *Water Resources Research*, 43(7), n/a-n/a.

852 Nijssen, B., D. P. Lettenmaier, X. Liang, S. W. Wetzler, and E. F. Wood (1997), Streamflow  
853 Simulation for Continental-Scale River Basins, *Water Resources Research*, 33(4),  
854 711-724.

855 Paniconi, C., P. A. Troch, E. E. Van Loon, and A. G. J. Hilberts (2003), Hillslope-Storage  
856 Boussinesq Model for Subsurface Flow and Variable Source Areas Along Complex  
857 Hillslopes: 2. Intercomparison with a Three-Dimensional Richards Equation Model,  
858 *Water Resources Research*, 39(11), n/a-n/a.

859 Polubarinova-Koch, P. I. (2015), *Theory of Ground Water Movement*, Princeton University  
860 Press.

861 Rinaudo, J.-D. (2015), Long-Term Water Demand Forecasting, edited, pp. 239-268, Springer  
862 Netherlands.

863 Rorabaugh, M. (1964), Estimating Changes in Bank Storage and Ground-Water  
864 Contribution to Streamflow: Extract of Publication No. 63 of the IASH Symposium  
865 Surface Waters.

866 Rupp, D. E., and J. S. Selker (2005), Drainage of a Horizontal Boussinesq Aquifer with a  
867 Power Law Hydraulic Conductivity Profile, *Water Resources Research*, 41(11), n/a-  
868 n/a.

869 Rupp, D. E., and J. S. Selker (2006), On the Use of the Boussinesq Equation for Interpreting  
870 Recession Hydrographs from Sloping Aquifers, *Water Resources Research*, 42(12),  
871 n/a-n/a.

872 Salas, F. R., M. A. Somos-Valenzuela, A. Dugger, D. R. Maidment, D. J. Gochis, C. H. David, W.  
873 Yu, D. Ding, E. P. Clark, and N. Noman (2018), Towards Real-Time Continental Scale  
874 Streamflow Simulation in Continuous and Discrete Space, *JAWRA Journal of the*  
875 *American Water Resources Association*, 54(1), 7-27.

876 Savenije, H. H., and P. Van der Zaag (2008), Integrated Water Resources Management:  
877 Concepts and Issues, *Physics and Chemistry of the Earth, Parts A/B/C*, 33(5), 290-  
878 297.

879 Schwarz, G. E., S. E. Jackson, and M. E. o. Wieczorek (2018), Select Attributes for Nhdplus  
880 Version 2.1 Reach Catchments and Modified Network Routed Upstream Watersheds  
881 for the Conterminous United States, edited by U. S. G. Survey.

882 Seo, Y. S., J. Šimůnek, and E. P. Poeter (2007), Documentation of the Hydrus Package for  
883 Modflow-2000, the U.S. Geological Survey Modular Ground-Water Model, Ground  
884 Water Modeling Center.

885 Shaw, S. B., and S. J. Riha (2012), Examining Individual Recession Events Instead of a Data  
886 Cloud: Using a Modified Interpretation of  $Dq/Dt-Q$  Streamflow Recession in  
887 Glaciated Watersheds to Better Inform Models of Low Flow, *Journal of Hydrology*,  
888 434-435, 46-54.

889 Shen, C., J. Niu, and M. S. Phanikumar (2013), Evaluating Controls on Coupled Hydrologic  
890 and Vegetation Dynamics in a Humid Continental Climate Watershed Using a  
891 Subsurface-Land Surface Processes Model, *Water Resources Research*, 49(5), 2552-  
892 2572.

893 Shen, C. P., and M. S. Phanikumar (2010), A Process-Based, Distributed Hydrologic Model  
894 Based on a Large-Scale Method for Surface-Subsurface Coupling, *Advances in Water*  
895 *Resources*, 33(12), 1524-1541.

896 Shin, Y., B. P. Mohanty, and A. V. M. Ines (2013), Estimating Effective Soil Hydraulic  
897 Properties Using Spatially Distributed Soil Moisture and Evapotranspiration, *Vadose*  
898 *Zone Journal*, 12(3), vzt2012.0094.

899 Stoelzle, M., K. Stahl, and M. Weiler (2013), Are Streamflow Recession Characteristics  
900 Really Characteristic?, *Hydrology and Earth System Sciences*, 17(2), 817-828.

901 Szilagyi, J., M. B. Parlange, and J. D. Albertson (1998), Recession Flow Analysis for Aquifer  
902 Parameter Determination, *Water Resources Research*, 34(7), 1851-1857.

903 Tallaksen, L. M. (1995), A Review of Baseflow Recession Analysis, *Journal of Hydrology*,  
904 165(1-4), 349-370.

905 Tashie, A., T. Pavelsky, and L. E. Band (2020), An Empirical Reevaluation of Streamflow  
906 Recession Analysis at the Continental Scale, *Water Resources Research*, 56(1).

- 907 Tesfa, T. K., H. Y. Li, L. R. Leung, M. Huang, Y. Ke, Y. Sun, and Y. Liu (2014), A Subbasin-Based  
 908 Framework to Represent Land Surface Processes in an Earth System Model,  
 909 *Geoscientific Model Development*, 7(3), 947-963.
- 910 Tijerina, D., L. Condon, K. Fitzgerald, A. Dugger, M. M. O'Neill, K. Sampson, D. Gochis, and R.  
 911 Maxwell (2021), Continental Hydrologic Intercomparison Project, Phase 1: A Large-  
 912 Scale Hydrologic Model Comparison over the Continental United States, *Water*  
 913 *Resources Research*, 57(7).
- 914 Troch, P. A., F. P. De Troch, and W. Brutsaert (1993), Effective Water Table Depth to  
 915 Describe Initial Conditions Prior to Storm Rainfall in Humid Regions, *Water*  
 916 *Resources Research*, 29(2), 427-434.
- 917 Troch, P. A., C. Paniconi, and E. Emiel Van Loon (2003), Hillslope-Storage Boussinesq Model  
 918 for Subsurface Flow and Variable Source Areas Along Complex Hillslopes: 1.  
 919 Formulation and Characteristic Response, *Water Resources Research*, 39(11), n/a-  
 920 n/a.
- 921 Troch, P. A., et al. (2013), The Importance of Hydraulic Groundwater Theory in Catchment  
 922 Hydrology: The Legacy of Wilfried Brutsaert and Jean-Yves Parlange, *Water*  
 923 *Resources Research*, 49(9), 5099-5116.
- 924 Vannier, O., I. Braud, and S. Anquetin (2014), Regional Estimation of Catchment-Scale Soil  
 925 Properties by Means of Streamflow Recession Analysis for Use in Distributed  
 926 Hydrological Models, *Hydrological Processes*, 28(26), 6276-6291.
- 927 Viterbo, F., K. Mahoney, L. Read, F. Salas, B. Bates, J. Elliott, B. Cosgrove, A. Dugger, D.  
 928 Gochis, and R. Cifelli (2020), A Multiscale, Hydrometeorological Forecast Evaluation  
 929 of National Water Model Forecasts of the May 2018 Ellicott City, Maryland, Flood, *J.*  
 930 *Hydrometeorol.*, 21(3), 475-499.
- 931 Vogel, R. M., and C. N. Kroll (1992), Regional Geohydrologic-Geomorphic Relationships for  
 932 the Estimation of Low-Flow Statistics, *Water Resources Research*, 28(9), 2451-  
 933 2458.
- 934 Wagener, T., M. Sivapalan, P. Troch, and R. Woods (2007), Catchment Classification and  
 935 Hydrologic Similarity, *Geography Compass*, 1(4), 901-931.
- 936 Wang, D. (2011), On the Base Flow Recession at the Panola Mountain Research Watershed,  
 937 Georgia, United States, *Water Resources Research*, 47(3), n/a-n/a.
- 938 Wieczorek, M., and A. E. LaMotte (2010), Attributes for Nhdplus Catchments (Version 1.1)  
 939 for the Conterminous United States: Statsgo Soil Characteristics, *Report Rep. 490-*  
 940 *26*, Reston, VA.
- 941 Wu, R., X. Chen, G. Hammond, G. Bisht, X. Song, M. Huang, G.-Y. Niu, and T. Ferre (2021),  
 942 Coupling Surface Flow with High-Performance Subsurface Reactive Flow and  
 943 Transport Code Pflotran, *Environmental Modelling & Software*, 137, 104959.
- 944 Zhao, T., X. Cai, and D. Yang (2011), Effect of Streamflow Forecast Uncertainty on Real-Time  
 945 Reservoir Operation, *Advances in Water Resources*, 34(4), 495-504.
- 946 Zhu, J., and B. P. Mohanty (2003), Effective Hydraulic Parameters for Steady State Vertical  
 947 Flow in Heterogeneous Soils, *Water Resources Research*, 39(8), n/a-n/a.

948

949

950 **List of Tables**

951 Table 1. Physics Differences in the Representation Scheme for the Aquifer (Subsurface) System  
952 between the Original NWM (i.e., NLSR Module) and the Presented NWM-BE3S model (i.e.,  
953 Boussinesq Aquifer Module). Except for the Aquifer Representation Scheme, All Other Physics  
954 Configurations were Preserved in the Newly Developed NWM-BE3S. .... 33

955 Table 2. Primary Physical Characteristics of the Selected 40 Catchments (Distributed over the  
956 Studied Three Major Basins). (\* data derived from the NWM input, \*\* from the STATSGO2) 34

957 Table 3. Recession Parameters for Each Time Domain (i.e., Early and Late Time) and Resulting  
958 Determined Effective Aquifer Properties on Catchment-Scale for the Selected 40 Catchments. 35

959

960

961

962

963

964

965

966

967

968

969

970

971

972

973

974

975

976 Table 1. Physics Differences in the Representation Scheme for the Aquifer (Subsurface) System  
 977 between the Original NWM (i.e., NLSR Module) and the Presented NWM-BE3S model (i.e.,  
 978 Boussinesq Aquifer Module). Except for the Aquifer Representation Scheme, All Other Physics  
 979 Configurations were Preserved in the Newly Developed NWM-BE3S.

Representation Scheme for The Aquifer(s) and GW-SW Exchanges	The NWM	The NWM-BE3S
Model Physics	<b>Exponential Functionality</b> between Bucket Height ( $z$ ) and Baseflow Fluxes $B_f$ (Equation 7)	<b>The Boussinesq Equation-Based</b> Catchment-Scale Lateral Groundwater Flow (Equation 1, and 2)
Parameters	<b>Empirical Parameters</b> -Two Fitting Parameters $C$ and $Exp$ - $Z_{max}$ to Define the Storage Capacity of the Conceptual Bucket	<b>Physical Parameters</b> -Horizontal Saturated Hydraulic Conductivity ( $K_s$ ) -Effective (Drainable) Porosity ( $f$ )
Resolution	Aggregated on Catchment-Scale	Lateral Resolution 50-m
Module Input & Output	<p>Soil Module (Noah-MP LSM)</p> <p>Soil Bottom Drainage</p> <p>Conceptual Single Bucket Module</p> <p>Baseflow Fluxes (<math>B_f</math>)</p> <p>Channel Routing Module</p> <p>One-Way Fluxes</p>	<p>Soil Module (Noah-MP LSM)</p> <p>Channel Routing Module</p> <p>Soil Bottom Drainage</p> <p>River Stage</p> <p>Boussinesq Aquifer Module</p> <p>Exchange Fluxes (<math>f_{pr}</math>)</p> <p>Two-Way Fluxes</p>

980 Table 2. Primary Physical Characteristics of the Selected 40 Catchments (Distributed over the  
 981 Studied Three Major Basins). (\* data derived from the NWM input, \*\* from the STATSGO2)

Basin	USGS Gage Number	Area (km <sup>2</sup> )	Total Stream Length (km)	Stream Order	Channel Bottom Width (m)*	Catchment Average Permeability (ms <sup>-1</sup> )**
Trinity River Basin	08048543	0.52	0.91	5	29.59	0.7
	084956950	11.18	5.39	2	9.17	3.31
	08064100	16.57	8.89	4	19.70	0.55
	08065800	1.59	1.39	5	14.54	1.57
	08063562	12.59	15.58	4	15.33	0.51
	08062500	10.07	18.17	6	43.19	0.5
	08062700	70.14	25.73	6	43.90	0.74
	08055560	39.46	7.42	6	29.12	1.44
	08045550	33.27	10.94	5	27.16	1.3
	08048000	3.81	3.70	5	29.33	0.9
	08049300	8.20	4.92	5	30.67	0.9
	08049500	8.51	6.31	5	30.96	0.87
	08057000	3.95	5.70	6	39.17	0.51
	08065000	3.90	2.37	6	50.49	0.57
08065350	1.34	2.69	6	51.82	0.23	
Brazos River Basin	08082000	0.75	0.37	5	34.02	1.36
	08091000	13.52	6.80	7	59.10	1.96
	08093100	36.90	7.23	7	60.47	2.16
	08162000	4.69	3.99	6	72.78	0.81
	08108700	12.60	1.33	7	70.04	1.48
	08111500	4.16	3.61	7	73.29	0.29
	08111850	19.17	7.04	7	73.76	0.53
	08114000	8.41	7.96	7	73.99	1.23
	08095300	26.08	4.34	3	12.07	0.71
	08104300	8.17	3.27	3	10.81	0.49
	08099382	10.36	6.87	3	11.04	1.05
	08090800	2.97	1.69	7	58.51	2.14
	08088610	9.42	3.90	7	56.83	1.36
08116650	2.53	3.71	7	74.19	1.24	
Colorado River Basin	08159200	1.95	2.06	6	71.42	1.31
	08159500	1.03	1.41	6	71.75	1.3
	08161000	8.89	5.34	6	72.54	1.92
	08143600	0.47	1.12	5	27.14	0.42
	08123850	3.36	2.76	6	47.97	2.12
	08136700	14.35	6.09	6	58.57	1.7
	08109700	14.42	6.09	4	13.05	1.39
	08158380	26.42	9.83	2	3.75	1.55
	08160800	10.21	5.41	2	5.50	5.45
	08155300	3.65	3.14	3	10.22	0.82
08158970	4.28	4.73	4	6.34	0.74	

982 Table 3. Recession Parameters for Each Time Domain (i.e., Early and Late Time) and Resulting  
 983 Determined Effective Aquifer Properties on Catchment-Scale for the Selected 40 Catchments.

Basin	$\text{Log}(a)$ (Early) (Fixed $b$ 3.0)	$\text{Log}(a)$ (Late) (Fixed $b$ 1.5)	$K_s$ ( $\text{ms}^{-1}$ )	$f$ (%)	Initial Aquifer Thickness $D_{ini}$ (m)	The size of Contributing Aquifer ( $\text{km}^2$ )
Trinity River Basin	-3.36	-1.78	4.80E-04	2.18E-01	45.3	1.77E-02
	-3.77	-1.89	8.82E-03	4.01E+00	0.6	9.06E-01
	-6.86	-2.58	4.81E-03	2.18E+00	7.4	1.52E+00
	-4.15	-1.97	4.42E-03	2.01E+00	3.8	1.30E-01
	-5.19	-2.39	4.12E-03	1.87E+00	2.1	3.53E-01
	-7.61	-3.26	2.38E-04	1.08E-01	60.9	6.75E-01
	-7.55	-3.22	4.28E-03	1.95E+00	8	4.35E+00
	-5.89	-2.49	9.99E-03	4.54E+00	2.3	2.45E+00
	-3.32	-2.16	8.70E-03	3.95E+00	0.3	9.32E-01
	-4.56	-2.78	2.73E-03	1.24E+00	7.5	3.20E-01
	-6.61	-3.15	2.80E-03	1.27E+00	29.5	3.69E-01
	-6.61	-3.05	3.01E-03	1.37E+00	24.4	4.34E-01
	-7.15	-3.13	2.66E-04	1.21E-01	89.2	3.67E-01
	-7.81	-3.25	8.24E-04	3.75E-01	182.1	1.17E-01
-8.02	-3.46	1.01E-05	4.61E-03	848	9.65E-02	
Brazos River Basin	-4.2	-1.75	5.93E-03	2.70E+00	5.9	1.88E-02
	-4.3	-2.15	8.27E-03	3.76E+00	0.7	1.24E+00
	-5.32	-2.61	9.67E-03	4.39E+00	1.4	3.32E-01
	-8.1	-3.2	6.41E-04	2.91E-01	174.8	2.81E-02
	-7.68	-3.29	4.58E-03	2.08E+00	54.1	1.26E-02
	-8.65	-3.47	1.57E-04	7.13E-02	455	4.16E-03
	-8.81	-3.3	3.84E-03	1.75E+00	86	1.55E+00
	-9	-3.25	7.42E-04	3.37E-01	209.6	7.57E-01
	-5.95	-2.67	9.79E-03	4.45E+00	2.9	2.14E+00
	-5.08	-2.69	4.37E-03	1.99E+00	4.5	2.61E-01
	-3.43	-2.21	5.60E-03	2.54E+00	0.5	9.22E-01
	-6.47	-2.83	3.78E-03	1.72E+00	45.1	2.23E-01
-6.4	-3.3	3.49E-03	1.58E+00	27.3	6.22E-01	
-8.9	-3.3	1.49E-04	6.78E-02	472	1.14E-01	
Colorado River Basin	-7.98	-3.29	1.14E-04	5.16E-02	442	1.31E-01
	-7.75	-3.42	1.93E-05	8.76E-03	854	3.50E-02
	-5.01	-2.6	4.19E-03	1.91E+00	3.5	1.51E-01
	-4.65	-2.27	5.96E-04	2.71E-01	29.7	1.69E-02
	-3.95	-2.07	4.69E-03	2.13E+00	1.8	3.12E-01
	-3.62	-2.16	9.54E-03	4.34E+00	0.4	1.15E-01
	-4.48	-2.44	6.07E-03	2.76E+00	1.1	7.21E-01
	-1.65	-1.62	5.99E-03	2.72E+00	0.2	5.28E-02
	-1.89	-1.64	1.04E-02	4.71E+00	0.14	5.92E-01
	-5.62	-2.61	3.82E-03	1.74E+00	13.6	2.96E-01
-2.37	-1.68	5.72E-03	2.60E+00	0.3	1.11E-01	

984 **List of Figures**

985 Figure 1. A Schematic of Boundary Condition-based Coupling Between River, Phreatic aquifer,  
986 and Vadose zone. (a) Euclidean Minimum Distance Map to Set Up Horizontal Profile of  
987 Temporary Aquifer Thickness  $E[D_i]$ , (b) Boundary Condition-Based Coupling Approach,  
988 Especially for Numerical Representation of Boussinesq Solutions under Transient River Stage  
989 Conditions during the Recession, (c) Soil Grid According to Time-Dependent Groundwater  
990 Level (GWL) using the Adaptive Volume Meshing (AVM) Technique, and (d) Hybrid Node-  
991 based Finite Volume and Difference Scheme. Adapted from “An Explicit Scheme to Represent  
992 the Bidirectional Hydrologic Exchanges Between the Vadose Zone, Phreatic Aquifer, and River”  
993 by *Hong et al.* [2020], Water Resources Research, by the American Geophysical Union. .... 38

994 Figure 2. Study Area Including the Entire Spatial Extent of the Trinity River Basin, the Brazos  
995 River Basin, and the Colorado River Basin Within Texas. 40 USGS Streamflow Gauges (i.e.,  
996 Trinity River Basin - 15 Gauges, Brazos River Basin - 14 Gauges, and Colorado River Basin - 11  
997 gauges) Were Selected to Assess the Improved Predictive Performance for Streamflow Due to  
998 the Implemented Boussinesq Aquifer Module in the NWM-BE3S Model. .... 39

999 Figure 3. Recession Analysis Plots in Bi-logarithmic Space for the Two Selected Gauges in Each  
1000 Studied Basin. The Examples Illustrate How the Recession Parameters  $a$  and  $b$  were Estimated  
1001 from Point Cloud data Using Lower Envelope (LE) Method. The Recession Parameters  $a$  and  $b$   
1002 Determined for the Respective Early and Late Time Domains were Used for Inferring Effective  
1003 Aquifer Properties on Catchment-Scale. .... 40

1004 Figure 4. (a) The Identified Linear Relationship Between Catchment Average Permeability  
1005 derived from STATSGO2 dataset and the Catchment-Scale Effective Horizontal Saturated  
1006 Hydraulic Conductivity ( $K_s$ ) (Estimated From Recession Analysis), (b) Probability Plots of  
1007 Diffusivity  $K_s/f$ . The Lognormal Distribution was Considered As the Most Appropriate  
1008 Probabilistic Distribution of  $K_s/f$  Derived From the 40 Selected Catchments/Gauges. .... 41

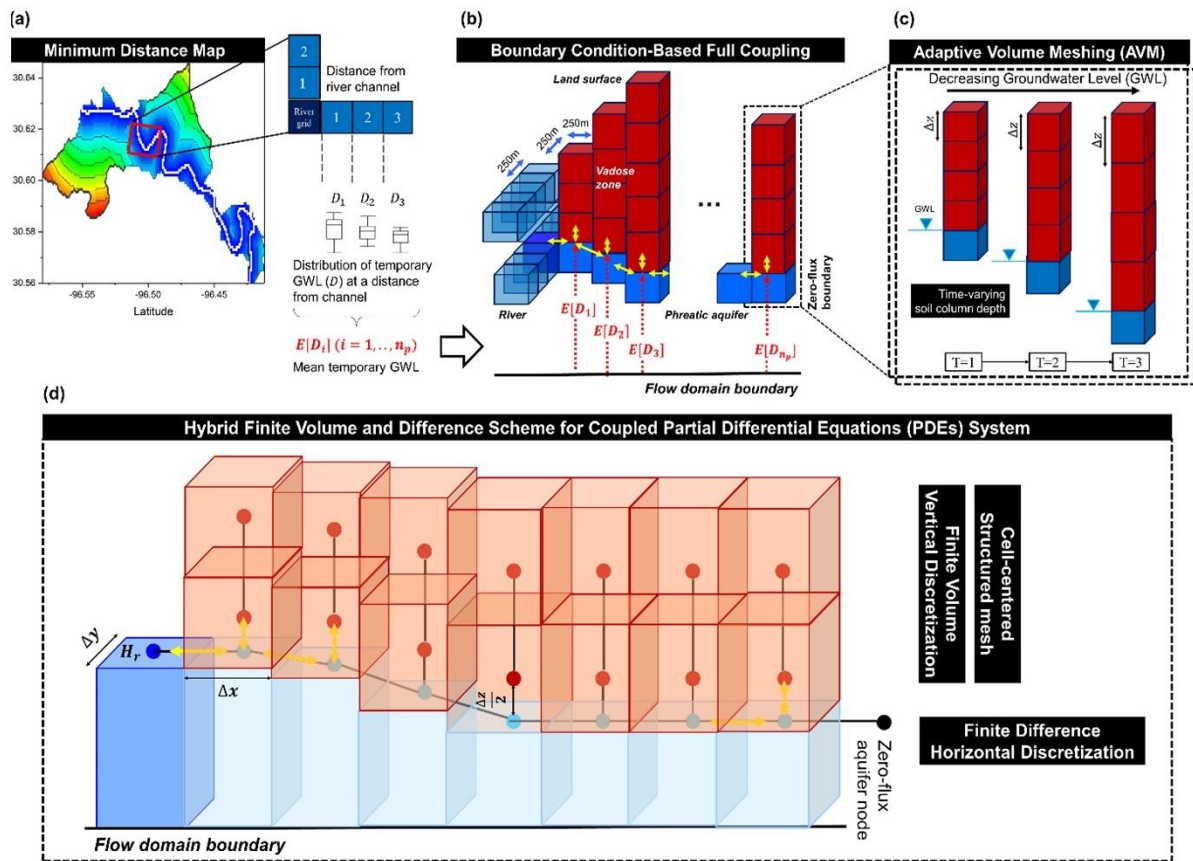
1009 Figure 5. Almost No Time Lags were Found Between the Soil Bottom Drainages Fluxes  
1010 (Modeled by the Noah-MP LSM) and Baseflow Fluxes in the Current NLSR Configuration From  
1011 the Selected 40 Catchments (a-1, a-2, b-1, b-2, c-1, c-2), (d) The (Almost) Identical Estimates  
1012 Between Cumulative Soil Drainage Fluxes and Baseflow Fluxes Exhibit the Lack of  
1013 Groundwater Storage in the NLSR(s). .... 42

1014 Figure 6. (a) The Temporal Agreement Between the Respective Baseflow Estimates from the  
1015 NWM and the NWM-BE3S was Found to be Related to the Linearity of the Streamflow  
1016 Recessions Observed in Corresponding Basin. Higher Agreements Between  $B_f$  and  $f_{pr}$  were  
1017 Identified as the Basin Functions More Like a Linear Reservoir, (b) The Relationship Between  
1018 the Temporal Correspondence Between  $B_f$  and  $f_{pr}$  (i.e., Pearson’s  $R$ ) and Recession Non-linearity  
1019 was Also Captured by a Non-linear Fitting (Power). .... 43

1020 Figure 7. Comparative Time Series of the  $B_f$  and  $f_{pr}$  Estimates for Two Catchments Showing  
1021 Contrasting Recession Non-linearity (i.e., Low or High) in the Streamflow Observations. The  
1022 Modeled Outflow Fluxes From the Boussinesq Aquifer ( $f_{pr}$ ) were Identified Able to Better  
1023 Represent the Baseflow Recessions with High Non-linearity than the NLSR model. .... 44

1024 Figure 8. The Improvements in the Streamflow Predictions Found in the NWM-BE3S model.  
1025 While Significant Improvements in  $R$  and Reductions in  $RMSE$  From All the Four-month

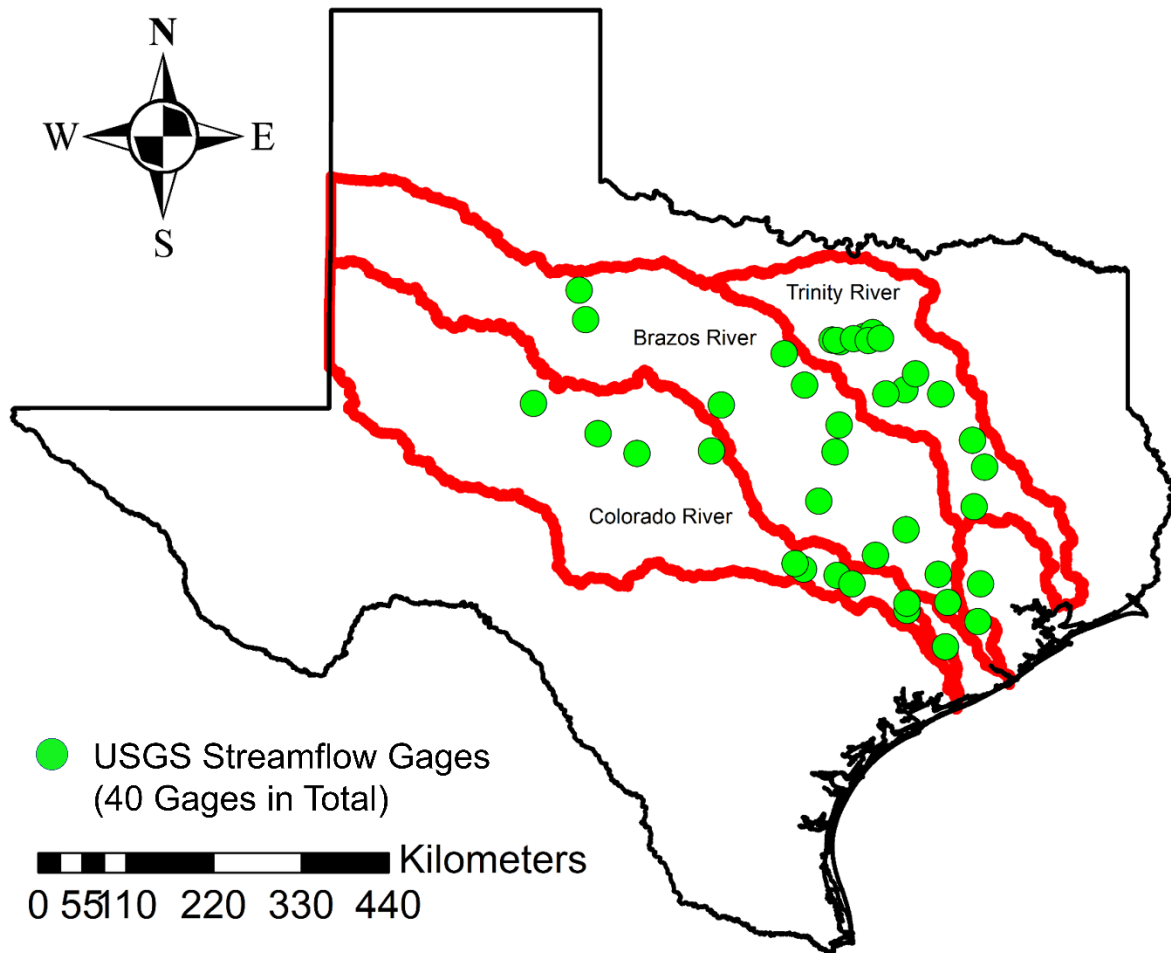
1026	Interval Periods (i.e., JFMA, MJJA, SOND), More Pronounced Improvements in <i>R</i> and <i>RMSE</i>	
1027	were Found As the Corresponding Basin Exhibited Low Non-linearities (i.e., Linearity,	
1028	Parameter <i>b</i> Close to 1.0). The Comparison of the Average and Value Distributions of <i>R</i> and	
1029	<i>RMSE</i> between the NWM and the NWM-BE3S Manifests the Technical Enhancement of Model	
1030	Structure. ....	45
1031	Figure 9. Comparative Time Series of Normalized Streamflow in Each Four-month Interval	
1032	Period and Evaluation against the Corresponding Streamflow Observations. As Expected from	
1033	the Improved Metrics <i>R</i> and <i>RMSE</i> in the NWM-BE3S, the Recession Durations and the Timings	
1034	of Peak Discharge were Better Predicted in the NWM-BE3S model Compared to the Original	
1035	NWM.....	46
1036	Figure 10. Comparative Evaluation of Recession Duration Errors in the Studied Catchments. The	
1037	NWM Identified That the Modeled Recession Duration were generally longer than the	
1038	(Corresponding) Actual Duration, and the Significant Reductions in the Duration Error were	
1039	Identified in the NWM-BE3S. ....	47
1040	Figure 11. Comparison Between (a) and (b) Shows: (1) Structural Limitation of the Current	
1041	NLSR model in the NWM that Cannot Depict Losing Conditions in the River Reaches, (2) The	
1042	Dominant Processes Between the River and the Aquifer were Spatially Heterogeneous Roughly	
1043	Following the Climatic Gradients over the Study Area. (c) About 10.1 % of the Total River	
1044	Reaches were Diagnosed as Losing Reaches While Showing the New Predictive Capabilities in	
1045	the NWM-BE3S to Represent Both River States (i.e., Either Gaining or Losing) Based on the	
1046	Bidirectional Lateral Hydraulic Connections Between the Stream and the Aquifer. ....	48
1047		
1048		
1049		
1050		
1051		
1052		



1053

1054 Figure 1. A Schematic of Boundary Condition-based Coupling Between River, Phreatic aquifer,  
 1055 and Vadose zone. (a) Euclidean Minimum Distance Map to Set Up Horizontal Profile of  
 1056 Temporary Aquifer Thickness  $E[D_i]$ , (b) Boundary Condition-Based Coupling Approach,  
 1057 Especially for Numerical Representation of Boussinesq Solutions under Transient River Stage  
 1058 Conditions during the Recession, (c) Soil Grid According to Time-Dependent Groundwater  
 1059 Level (GWL) using the Adaptive Volume Meshing (AVM) Technique, and (d) Hybrid Node-  
 1060 based Finite Volume and Difference Scheme. Adapted from “An Explicit Scheme to Represent  
 1061 the Bidirectional Hydrologic Exchanges Between the Vadose Zone, Phreatic Aquifer, and River”  
 1062 by *Hong et al.* [2020], *Water Resources Research*, by the American Geophysical Union.

1063



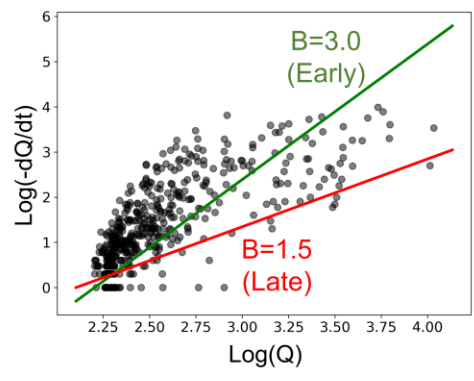
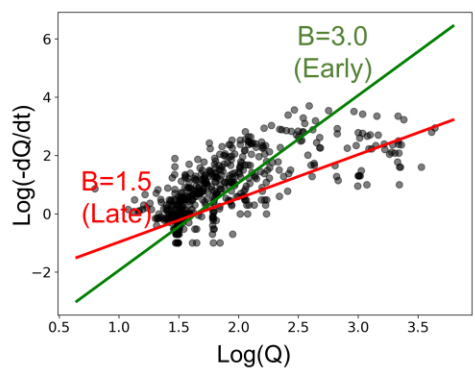
1064

1065 Figure 2. Study Area Including the Entire Spatial Extent of the Trinity River Basin, the Brazos  
 1066 River Basin, and the Colorado River Basin Within Texas. 40 USGS Streamflow Gauges (i.e.,  
 1067 Trinity River Basin - 15 Gauges, Brazos River Basin - 14 Gauges, and Colorado River Basin - 11  
 1068 gauges) Were Selected to Assess the Improved Predictive Performance for Streamflow Due to  
 1069 the Implemented Boussinesq Aquifer Module in the NWM-BE3S Model.

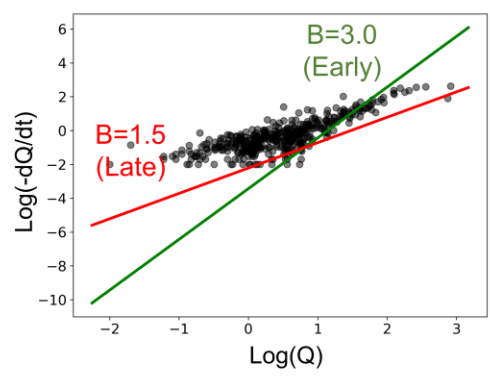
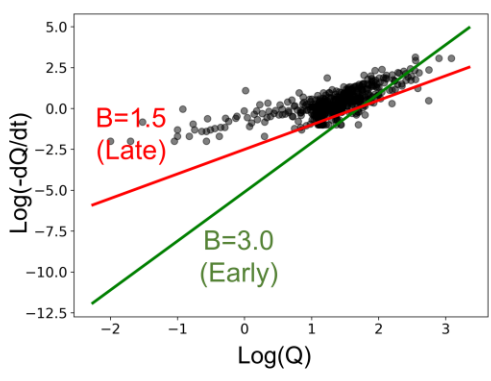
1070

1071

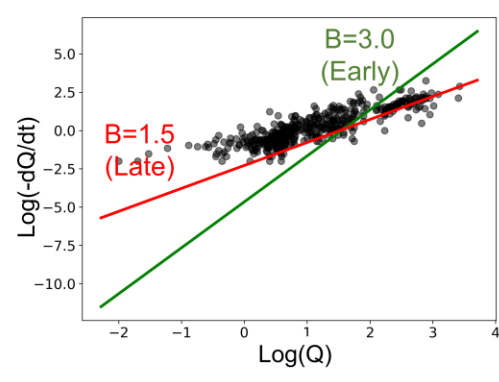
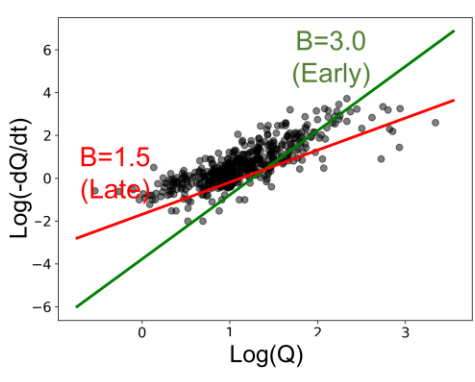
Trinity River Basin



Brazos River Basin

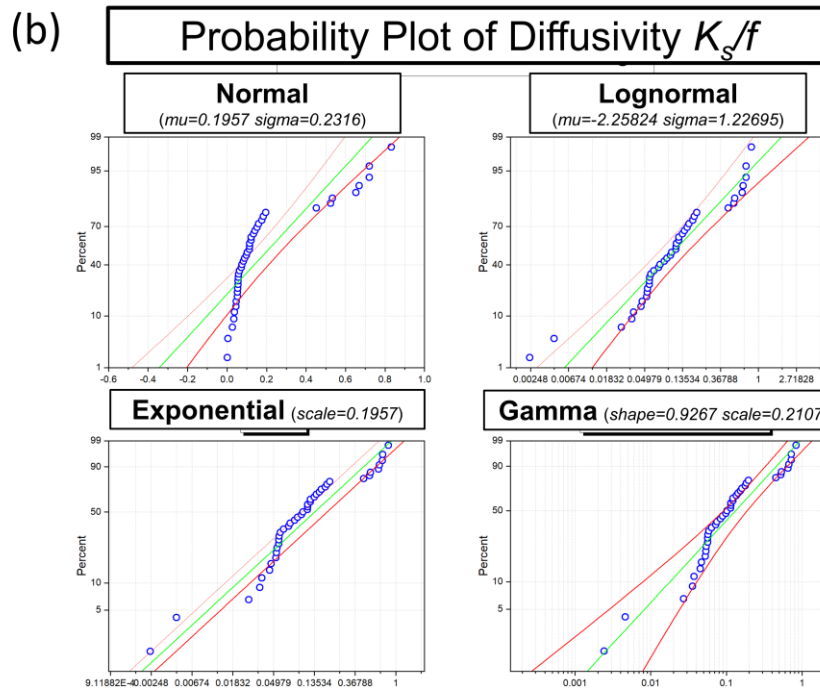
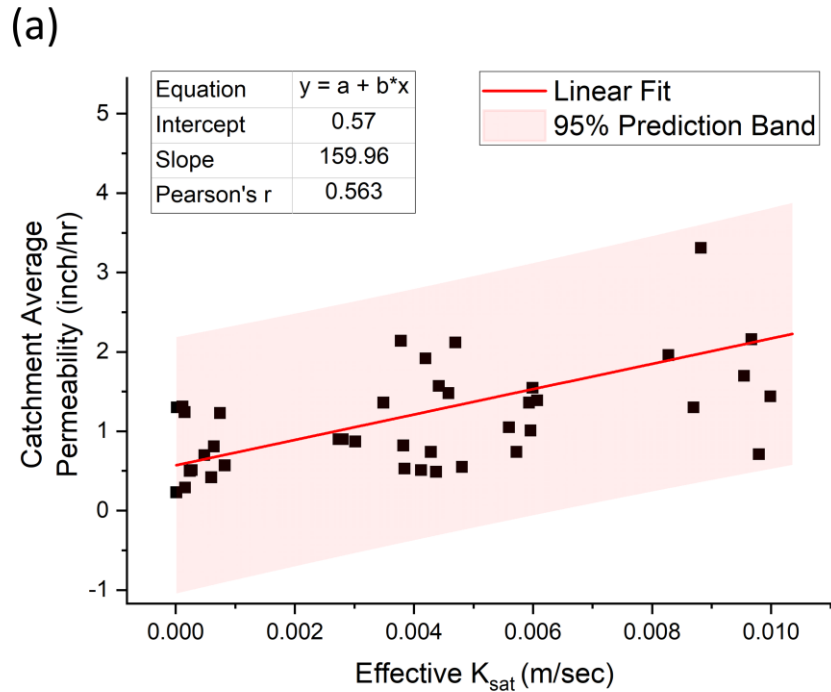


Colorado River Basin



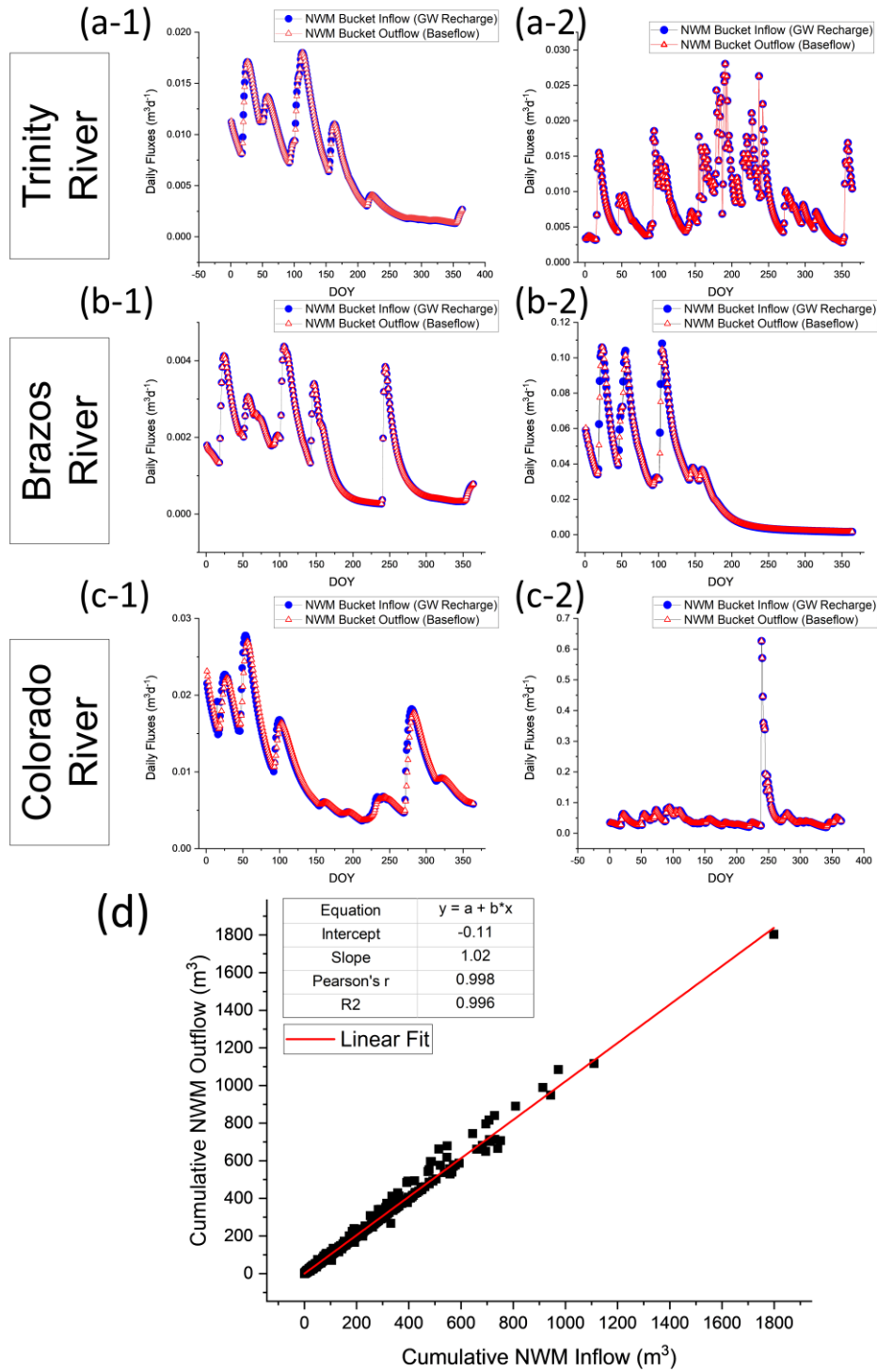
1072

1073 Figure 3. Recession Analysis Plots in Bi-logarithmic Space for the Two Selected Gauges in Each  
 1074 Studied Basin. The Examples Illustrate How the Recession Parameters  $a$  and  $b$  were Estimated  
 1075 from Point Cloud data Using Lower Envelope (LE) Method. The Recession Parameters  $a$  and  $b$   
 1076 Determined for the Respective Early and Late Time Domains were Used for Inferring Effective  
 1077 Aquifer Properties on Catchment-Scale.



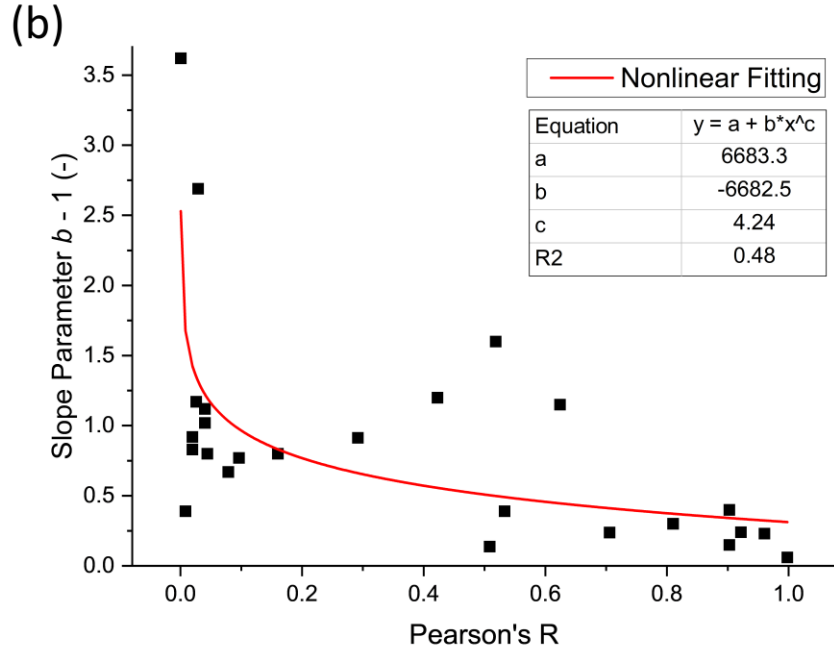
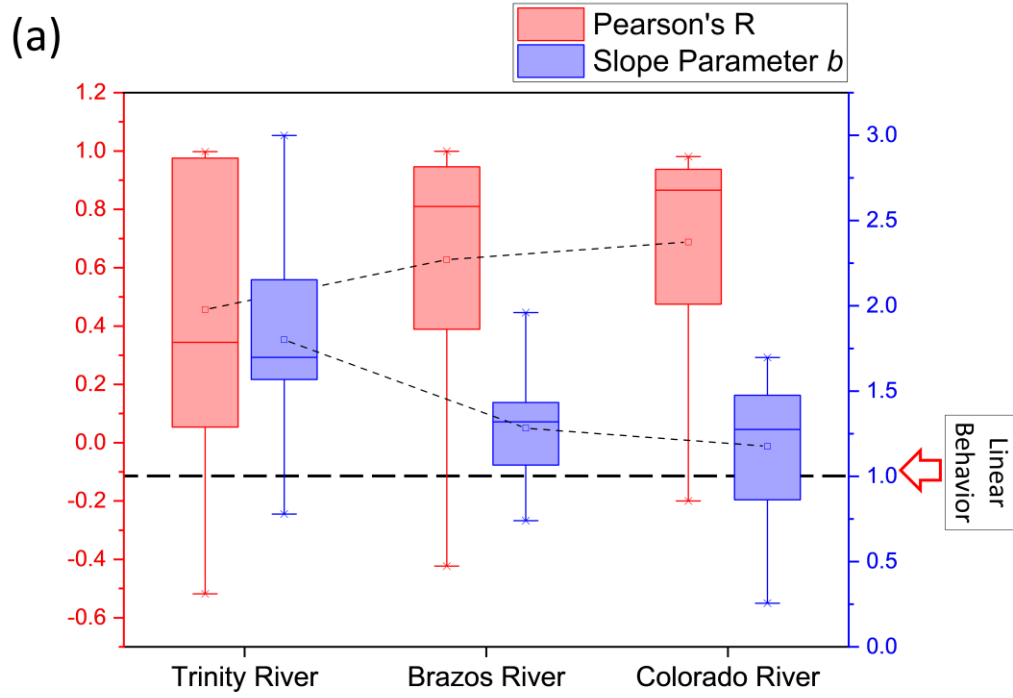
1078

1079 Figure 4. (a) The Identified Linear Relationship Between Catchment Average Permeability  
 1080 derived from STATSGO2 dataset and the Catchment-Scale Effective Horizontal Saturated  
 1081 Hydraulic Conductivity ( $K_s$ ) (Estimated From Recession Analysis), (b) Probability Plots of  
 1082 Diffusivity  $K_s/f$ . The Lognormal Distribution was Considered As the Most Appropriate  
 1083 Probabilistic Distribution of  $K_s/f$  Derived From the 40 Selected Catchments/Gauges.



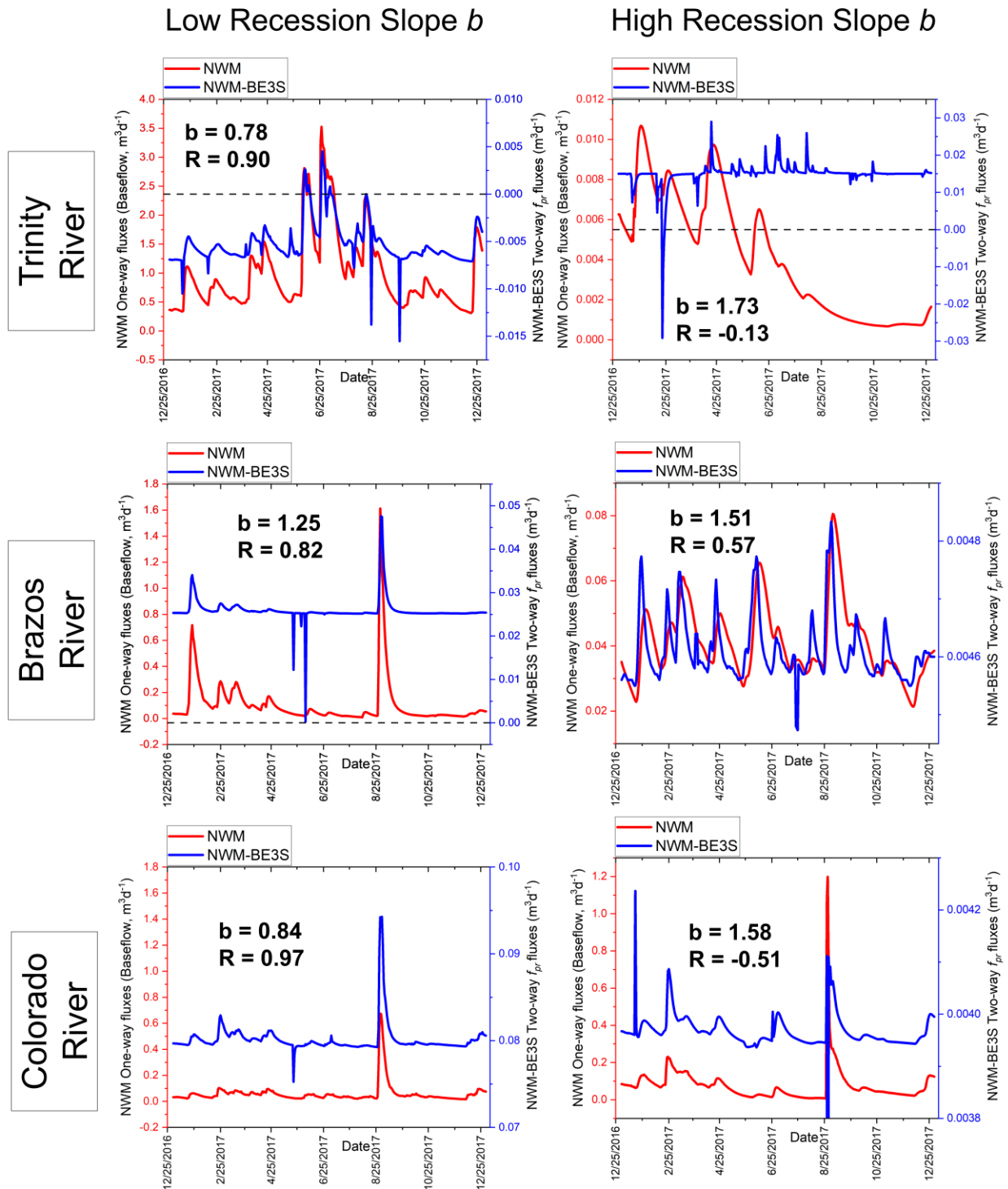
1084

1085 Figure 5. Almost No Time Lags were Found Between the Soil Bottom Drainages Fluxes  
 1086 (Modeled by the Noah-MP LSM) and Baseflow Fluxes in the Current NLSR Configuration From  
 1087 the Selected 40 Catchments (a-1, a-2, b-1, b-2, c-1, c-2), (d) The (Almost) Identical Estimates  
 1088 Between Cumulative Soil Drainage Fluxes and Baseflow Fluxes Exhibit the Lack of  
 1089 Groundwater Storage in the NLSR(s).



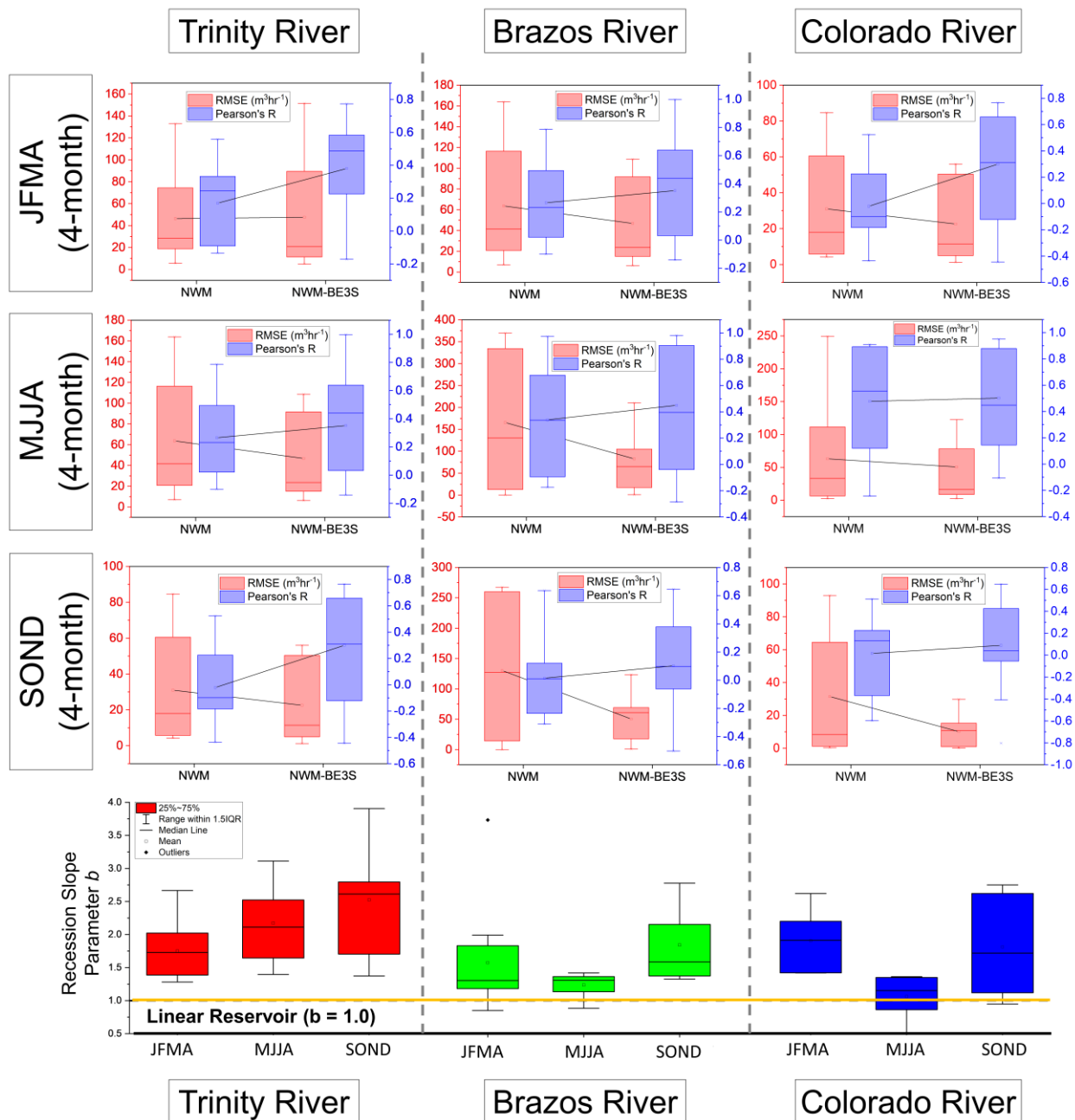
1090

1091 Figure 6. (a) The Temporal Agreement Between the Respective Baseflow Estimates from the  
 1092 NWM and the NWM-BE3S was Found to be Related to the Linearity of the Streamflow  
 1093 Recessions Observed in Corresponding Basin. Higher Agreements Between  $B_f$  and  $f_{pr}$  were  
 1094 Identified as the Basin Functions More Like a Linear Reservoir, (b) The Relationship Between  
 1095 the Temporal Correspondence Between  $B_f$  and  $f_{pr}$  (i.e., Pearson's  $R$ ) and Recession Non-linearity  
 1096 was Also Captured by a Non-linear Fitting (Power).



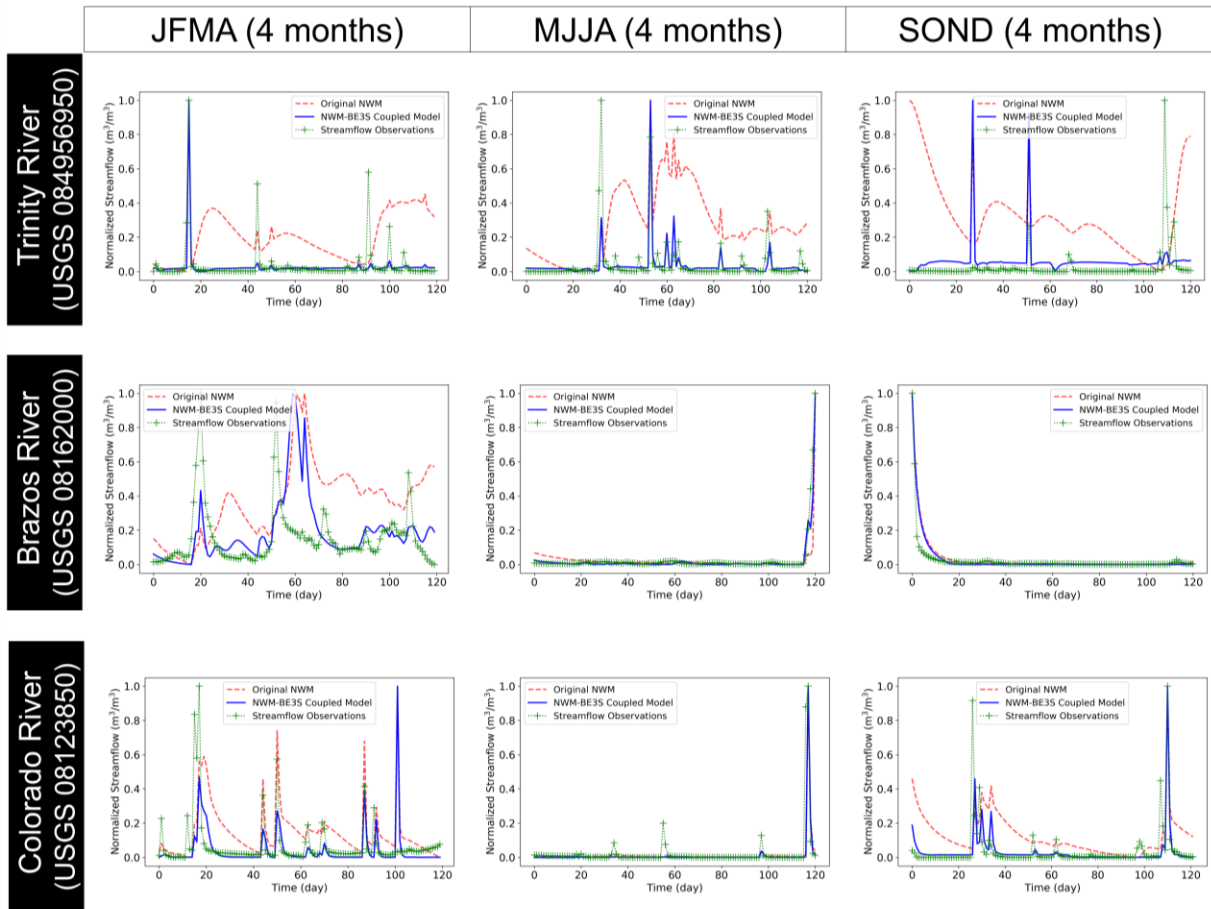
1097

1098 Figure 7. Comparative Time Series of the  $B_f$  and  $f_{pr}$  Estimates for Two Catchments Showing  
 1099 Contrasting Recession Non-linearity (i.e., Low or High) in the Streamflow Observations. The  
 1100 Modeled Outflow Fluxes From the Boussinesq Aquifer ( $f_{pr}$ ) were Identified Able to Better  
 1101 Represent the Baseflow Recessions with High Non-linearity than the NLSR model.



1102

1103 Figure 8. The Improvements in the Streamflow Predictions Found in the NWM-BE3S model.  
 1104 While Significant Improvements in  $R$  and Reductions in  $RMSE$  From All the Four-month  
 1105 Interval Periods (i.e., JFMA, MJJA, SOND), More Pronounced Improvements in  $R$  and  $RMSE$   
 1106 were Found As the Corresponding Basin Exhibited Low Non-linearities (i.e., Linearity,  
 1107 Parameter  $b$  Close to 1.0). The Comparison of the Average and Value Distributions of  $R$  and  
 1108  $RMSE$  between the NWM and the NWM-BE3S Manifests the Technical Enhancement of Model  
 1109 Structure.



1110

1111 Figure 9. Comparative Time Series of Normalized Streamflow in Each Four-month Interval  
 1112 Period and Evaluation against the Corresponding Streamflow Observations. As Expected from  
 1113 the Improved Metrics  $R$  and  $RMSE$  in the NWM-BE3S, the Recession Durations and the Timings  
 1114 of Peak Discharge were Better Predicted in the NWM-BE3S model Compared to the Original  
 1115 NWM.

1116

1117

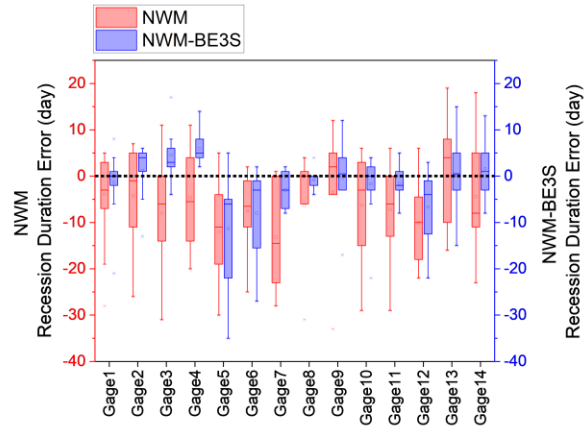
1118

1119

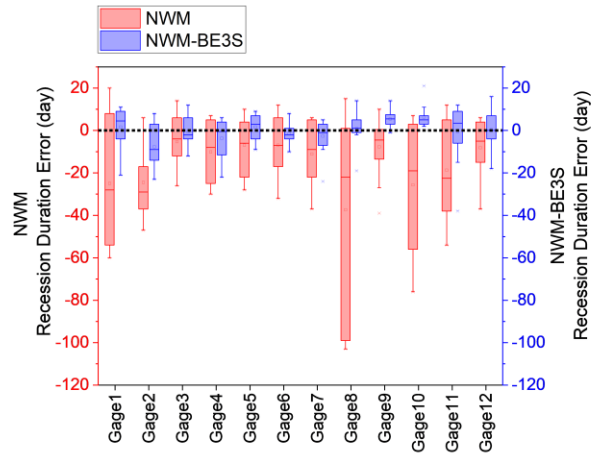
1120

1121

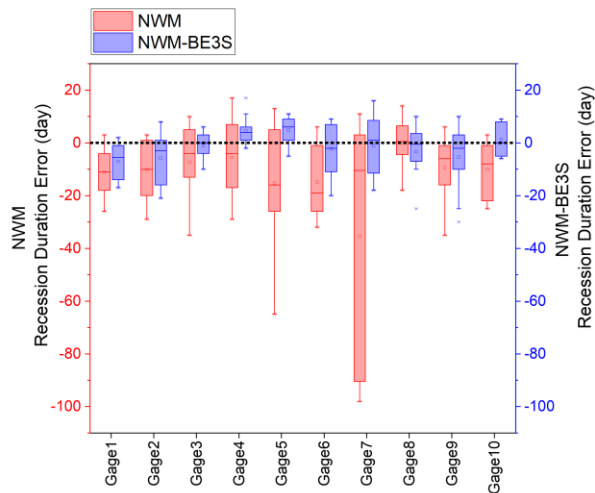
Trinity  
River



Brazos  
River

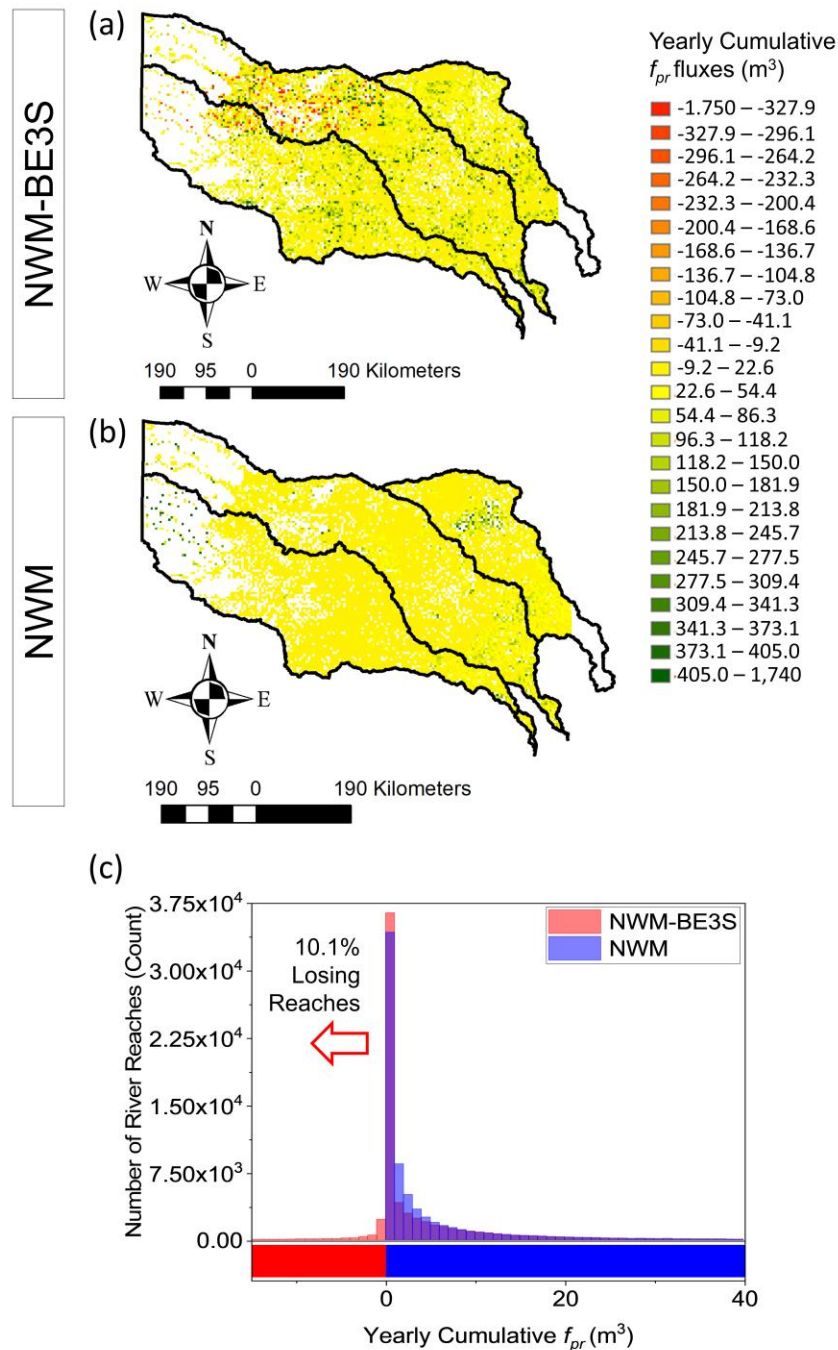


Colorado  
River



1122

1123 Figure 10. Comparative Evaluation of Recession Duration Errors in the Studied Catchments. The  
1124 NWM Identified That the Modeled Recession Duration were generally longer than the  
1125 (Corresponding) Actual Duration, and the Significant Reductions in the Duration Error were  
1126 Identified in the NWM-BE3S.



1127

1128 Figure 11. Comparison Between (a) and (b) Shows: (1) Structural Limitation of the Current  
 1129 NLSR model in the NWM that Cannot Depict Losing Conditions in the River Reaches, (2) The  
 1130 Dominant Processes Between the River and the Aquifer were Spatially Heterogeneous Roughly  
 1131 Following the Climatic Gradients over the Study Area. (c) About 10.1 % of the Total River  
 1132 Reaches were Diagnosed as Losing Reaches While Showing the New Predictive Capabilities in  
 1133 the NWM-BE3S to Represent Both River States (i.e., Either Gaining or Losing) Based on the  
 1134 Bidirectional Lateral Hydraulic Connections Between the Stream and the Aquifer.